

University of Alberta

Aerodynamic Aerosol Classifier

by

Farzan Tavakoli

A thesis submitted to the Faculty of Graduate Studies and Research
in partial fulfillment of the requirements for the degree of

Doctor of Philosophy

Department of Mechanical Engineering

©Farzan Tavakoli
Spring 2014
Edmonton, Alberta

Permission is hereby granted to the University of Alberta Libraries to reproduce single copies of this thesis and to lend or sell such copies for private, scholarly or scientific research purposes only. Where the thesis is converted to, or otherwise made available in digital form, the University of Alberta will advise potential users of the thesis of these terms.

The author reserves all other publication and other rights in association with the copyright in the thesis and, except as herein before provided, neither the thesis nor any substantial portion thereof may be printed or otherwise reproduced in any material form whatsoever without the author's prior written permission.

Abstract

A new aerosol particle classifier, the Aerodynamic Aerosol Classifier (AAC), is presented with some of its applications. The instrument uses a centrifugal force and sheath flow between two concentric rotating cylinders to produce a monodisperse aerosol classified by aerodynamic diameter. Since this instrument does not require charged particles, it produces a true monodisperse aerosol without artefacts caused by multiply-charged particles like other classifiers. This work reports the theoretical and experimental results of the new instrument with some of its applications. Two diffusion models and two non-diffusion models have been used to predict the performance of the AAC. The transfer functions were obtained as a function of the particle relaxation time and the particle aerodynamic diameter. The transfer function has been studied for different flow rates. PSL (polystyrene latex) particles and DOS (DioctylSebacate) along with a differential mobility analyzer (DMA) were used to verify the instrument and to obtain the experimental transfer function. A DMA and the AAC were used in tandem to measure the effective density, dynamic shape factor, and the mass of soot particles emitted from an inverted burner and DOS droplets.

Acknowledgements

I would like to express my heartfelt gratitude to my supervisor Dr. Jason Olfert, for all his support, and patience and also for providing me with this very interesting research project. He was friendly, involved and supportive every day.

I would like to thank the Mechanical Engineering staff in mechanic shop who helped me in manufacturing. I would also like to take this opportunity to thank colleagues and friends who support me over these years.

I would also like to acknowledge the support I have received from Cambustion Ltd. through their financial support, and their technical support. I am especially grateful to Dr. Jonathan Symonds for his technical supports and his expertise.

Finally, I would like to thank my father who taught me critical thinking and logic and my mother who I had her unconditional love and support. Likewise, I would like to express my gratitude to love of my life, Roxana who was patient and supportive during this work.

Table of Contents

Chapter 1: Introduction	1
1.1 Aerosol science and measurement:	1
1.2 Methods to measure aerodynamic size.....	3
1.3 Monodisperse classifiers	7
1.3.1 Differential mobility analyzer.....	7
1.3.2 Aerosol particle mass analyzer	10
1.3.3 Couette CPMA.....	11
1.4 Overview	11
Chapter 2: Theoretical Models of the Aerodynamic Aerosol Classifier	17
2.1 Working principle	18
2.2 Non-diffusion models.....	20
2.2.1 Limiting trajectory model	20
2.2.2 Particle streamline model.....	24
2.2.3 Discussion of non-diffusion models	26
2.3 Diffusion models	29
2.3.1 Convective diffusion model	30
2.3.2 Diffusing particle streamline model.....	33
2.3.3 Discussion of diffusion models.....	34
2.4 Conclusion and summary.....	39
Chapter 3: Experimental Validation of the Aerodynamic Aerosol Classifier	43

3.1	Introduction	43
3.2	Prototype	44
3.3	Experimental setups for examining transfer function	46
3.3.1	Examining transfer function shape using PSL.....	48
3.3.2	Examining transfer function shape using DOS.....	50
3.3.3	AAC efficiency using PSL.....	51
3.3.4	AAC efficiency using DOS	53
3.4	Experimental results and discussion	54
3.4.1	AAC Effective length	54
3.4.2	Experimental transfer function	55
3.4.3	Resolution	59
3.4.4	AAC Efficiency	60
3.5	Summary	62
Chapter 4: Determination of particle mass, effective density, mass-mobility exponent and dynamic shape factor using an aerodynamic aerosol classifier and a differential mobility analyzer in tandem.....		
		65
4.1	Introduction	65
4.2	Experimental setup.....	67
4.3	Results and discussion.....	70
4.3.1	Particle Mass.....	70
4.3.2	Effective density	72
4.3.3	Dynamic shape factor	74

4.4	Conclusion.....	77
Chapter 5: Conclusions and Future Work.....		83
5.1	Conclusions and discussion.....	84
5.1.1	Theoretical conclusions	84
5.1.2	Experimental conclusions	86
5.1.3	Soot particle measurement.....	86
5.2	Future work	87
Appendix A: Particle Relaxation Time as a Function of Aerodynamic Diameter		89
Appendix B: Geometric Factor for AAC.....		91
Appendix C: Aerosol Penetration in Microchannels		93
C.1	Introduction	94
C.2	Theory.....	97
C.3	Methodology.....	101
C.4	Results and discussion	102
C.4.1	Effect of slip flow at the walls on the penetration	102
C.4.2	Penetration equation.....	105
C.4.3	Nonzero particle concentration at the walls.....	107
C.5	Conclusion	109
Appendix D: Implementing the Crank-Nicolson Method for the Numerical Diffusion Model of AAC		113
Appendix E: Uncertainty Analysis		119

List of Figures

Figure 1. 1 inertial impactors: (a) plate impactor, (b) virtual impactor (Marple, 2004).	4
Figure 1. 2 conifuge (Poynting, 1972).	5
Figure 1. 3 Helical shaped channel of Goetz aerosol spectrometer (Goetz, 1957). 6	6
Figure 1. 4 schematic of the Aerosol and Particle Separator, LAPS (Cheng et al, 1988)	7
Figure 1. 5 Schematic of DMA.....	9
Figure 1. 6 Schematic of APM, aerosol particle mass analyzer.	10
Figure 2. 1 Schematic of the Aerodynamic Aerosol Classifier.	19
Figure 2. 2 Details of the particle trajectory and flows between the cylinders.....	19
Figure 2. 3 AAC transfer function for two non-diffusion models with balanced flows ($\delta=0$) and aerosol to sheath flow ratio of 0.1 ($\beta=0.1$). The solid line shows the particle streamline model, and dashed and dashed-dot lines represent the limiting trajectory model.....	27
Figure 2. 4 Transfer function of the AAC using the limiting trajectory model (thick lines) and particle streamline model (thin lines) for (a) unbalanced flows ($\delta \neq 0$) when $\beta = 0.1$ and (b) balanced flows ($\delta = 0$) at different aerosol to sheath flow ratios.	29
Figure 2. 5 AAC transfer function models with $\delta=0$ and $\beta=0.1$. The models include the non-diffusion limiting trajectory model (solid line), the convective diffusion model when the diffusion term is zero (dotted line), the diffusing particle streamline model (dashed-dot line), and the convective diffusion model (dashed line).....	36
Figure 2. 6 Resolution as a function of η^* and σ^* from the convective diffusion model and diffusing particle streamline model, respectively, for $\delta=0$ and $\beta=0.1$.	36

Figure 2. 7 Transfer functions calculated with the convective diffusion model ($\delta=0$ and $\beta=0.1$) of spherical particles with an aerodynamic diameter of (a) 30 nm, (b) 100 nm, (c) 300 nm with particle densities of 500, 1000 and 2000 kg/m ³ for the instrument specifications in Table 2.1.	38
Figure 3. 1 A schematic of the AAC prototype	45
Figure 3. 2 AAC flow diagram	46
Figure 3. 3 Setup to examine the AAC transfer function using known PSL size (setup I)	49
Figure 3. 4 Setup to examine the experimental transfer function with DOS (Setup II).....	50
Figure 3. 5 Setup to obtain the AAC efficiency (Setup III).....	52
Figure 3. 6 Experimental setup (IV)	53
Figure 3. 7 Calibration curve for the AAC, where τ is the particle relaxation time of PSL and DOS particles and τ^* is the expected instrument response from the theory. The error bars represent a 95% confidence interval in the uncertainty of the DMA (estimated to be 3%, Kinney <i>et al.</i> , 1991) and PSL spheres (~2–3% depending on size) and 3% in uncertainty in density of DOS.	55
Figure 3. 8 Normalized PSL particle concentration versus AAC rotational speed (setup I)	57
Figure 3. 9 Experimental and theoretical DOS concentration (setup II)	59
Figure 3. 10 AAC resolution using DOS with sample flow of 0.3 L/min and different sheath flow (setup II)	60
Figure 3. 11 AAC efficiency using DOS and PSL particles (setup III and IV)....	61
Figure 4. 1 Schematic diagram of the experimental setup.....	69
Figure 4. 2 Soot particle concentration at the exit of the AAC-DMA.....	70

Figure 4. 3 The particle mass-mobility relationship for (a) soot particles and (b) DOS particles.....	72
Figure 4. 4 Effective density of soot, DOS and PSL particles.....	74
Figure 4. 5 Shape factor of soot and DOS particles.....	77
Figure C. 1 Schematic of microchannels, (a) a rectangular microchannel and (b) a microtube.	98
Figure C. 2 Variation of wall slip correction for (a) rectangular microchannels and (b) microtubes for different values of μ . Marked ‘o’: results by applying the nonzero boundary condition for particle concentration at the walls (Gallis et al., 2008b).	104
Figure C. 3 Variation of penetration with deposition factor for (a) rectangular channels and (b) cylindrical tubes. Solid line: numerical results for the continuum regime, dashed line: Knudsen number equals 0.1, marked ‘o’: results by Bowen et al. (1976).	105
Figure C. 4 Variation of article concentration at the wall for (a) continuum regime and (b) Kn=0.1 for a rectangular microchannel.....	108

List of Tables:

Table 2.1 Proposed dimensions and operating conditions.....	26
---	----

List of Nomenclature

\mathbf{v}	particle velocity
\mathbf{u}	gas velocity
\mathbf{a}	centrifugal acceleration
u	gas velocity in z direction
v_{TS}	terminal settling velocity
m	particle mass
f	fraction of particles that pass through the classifier
n	particle concentration
\tilde{n}	non-dimensional particle concentration
C_c	slip correction factor
d_{ae}	aerodynamic equivalent diameter
d_{ae}^*	d_{ae} at the center of transfer function ($\tau = \tau^*$)
d_{ve}	volume equivalent diameter including internal voids
d_{mo}	mobility equivalent diameter
d_p	particle diameter
z	distance in the axial direction
r	distance from axis of rotation
r_1	inner cylinder radius
r_2	outer cylinder radius
r_{in}	initial position of the particle at the classifier entrance

\bar{r}	$= (r_1 + r_2)/2$
r_c	critical radius
r_a	aerosol flow streamline radius
r_s	sample flow streamline radius
\tilde{r}	non-dimensional radius (r/h)
\tilde{z}	non-dimensional length (z/L)
Q_{sh}	sheath flow rate
Q_a	aerosol flow rate
Q_{exh}	exhaust flow rate
Q_s	sample flow rate
B	mechanical mobility
D	diffusion coefficient
D_{fm}	mass-mobility exponent
L	classifier length
T	temperature
R	classifier resolution
h	radial distance between two cylinders ($r_2 - r_1$)
\tilde{h}	$= h/\bar{r}$
η	non-dimensional number defining diffusion effect in convective diffusion model
η_{AAC}	AAC penetration efficiency

η^*	η at the center of transfer function ($\tau = \tau^*$)
ζ	non-dimensional number defining transfer function location
k	Boltzmann's constant
τ	relaxation time
τ_{\max}	largest τ that passes through the classifier
τ_{\min}	smallest τ that passes through the classifier
$\Delta \tau$	$= (\tau_{\max} - \tau_{\min})/2$
τ^*	τ at the maximum of the transfer function
$\tilde{\tau}$	dimensionless particle relaxation time ($\tilde{\tau} = \tau/\tau^*$)
ω	rotational speed
μ	gas dynamic viscosity
ρ_p	particle density including internal voids
ρ_0	standard density (1000 kg/m ³)
ρ_{eff}	effective density
Z_p	electrical mobility
F_D	drag force
Ω	transfer function
χ	dynamic shape factor
G_{AAC}	non-dimensional geometry factor of AAC
δ	$= Q_s - Q_a/Q_s + Q_a$
β	$= Q_s + Q_a/Q_{\text{sh}} + Q_{\text{exh}}$

σ	non-dimensional number defining diffusion effect in streamline model
σ^*	σ at the center of transfer function ($\tau = \tau^*$)
$\varepsilon(x)$	$= x \cdot \text{erf}(x) + e^{x^2} / \sqrt{\pi}$ and $\text{erf}(x)$ is the error function
FWHM	full-width half maximum of transfer function
PSL	polystyrene latex
DOS	DioctylSebacate
APM	aerosol particle mass Analyzer
CPC	condensation particle counter
CPMA	centrifugal particle mass analyzer
DMA	differential mobility analyzer
ELPI	electrical low pressure impactor
TEM	transmission electron microscope
LT	limiting trajectory (model)
CD	convective diffusion (model)
PS	particle streamline (model)
DPS	diffusing particle streamline (model)

Chapter 1

Introduction

1.1 Aerosol science and measurement:

Aerosols are a suspension of liquid or solid particles in a gas. They are formed either by gas-to-particle conversion or by the disintegration of solids or liquids. Aerosols are ubiquitous in the Earth's atmosphere. For example, many common phenomena such as smoke and dust can be described as high concentrations of aerosols. Aerosol particles can have a variety of different sizes, shapes, densities and chemical components.

The history of aerosol science goes back to early air pollution studies, such as the detection of harmful particles in the air (Spurny, 1998). The importance of aerosol characterization has been highlighted by studies on the effect of industrial aerosols on human health and in the workplace in the 1950s (Baron and Willeke 2001). More recently, aerosol measurement is required for various fields including global warming, nanotechnology, chemical manufacturing, pharmaceuticals, and drug delivery.

Particle size, number concentration and chemical composition are important aerosol properties. Particle size can largely determine their behavior in a gas. The concept of spherical particle size is unambiguous (i.e. it can be defined by its diameter or radius); however, for non-spherical particles, with a variety of shapes, this term must be defined. Therefore the concept of equivalent diameter is used to describe the particle size when the particles are non-spherical. Every equivalent diameter is defined according to a specific physical property or measurement technique. Aerodynamic equivalent diameter, mobility equivalent diameter, volume equivalent diameter, mass equivalent diameter, envelop equivalent diameter, projected area equivalent diameter and Sauter mean diameter are the most well-known definitions (Kulkarni et al. 2011).

Most naturally-produced aerosols are polydispersed (i.e. are comprised of particles with a wide range of sizes) and cover more than two orders of magnitude in size. Therefore the size of aerosol particles are characterized by statistical concepts. Particle size distributions show the variation of a specific aerosol property (for example particle number concentration or mass) over a size range of interest, and often follow a logarithmic normal distribution. However, atmospheric and combustion aerosols often have a bimodal distribution, which is a result of two different particle generation mechanisms.

The period of aerosol science before 1960 is referred to as classical aerosol physics. In that time there was no laser, computer or spectroscopy tools available (Spurny, 1998). Aerosol measurement was usually based on using a microscope. Particles were collected and then counted according to their size, mainly in the range of 0.5 to 5 μm . Since the sampling and analysis process could last for several hours, particles experienced rebound and deagglomeration,

resulting in a substantially high measurement error (Baron and Willeke 2001, Kulkarni et al. 2011).

1.2 Methods to measure aerodynamic size

The aerodynamic equivalent diameter is defined as the diameter of a spherical particle with unit density that has the same terminal settling velocity as the actual particle. Except for very irregular particles in a shear flow, particles with the same aerodynamic diameter follow the same path in a flow. Therefore if the aerodynamic diameter of a particle is known, diffusion effects are neglected and no phoretic forces are present, the motion of the particle can be described independently of its morphology and density.

In order to separate a specific particle size an external force is required. External forces, such as gravity or electrostatic forces cause the particle to move in the force field. The relative particle velocity to the gas flow velocity is called the migration velocity, which depends on the particle size. This force is often used for particle-size classification. The principle of particle inertial classification is based on using particle inertia to separate or classify particles by their size. Large particles with high inertia tend to cross gas streamlines, but small particles with less inertia remain in the gas flow. Current instruments using particle inertia for classification are impactors, virtual impactors, and cyclones (Baron and Willeke, 2001).

Impactors are simple devices, where aerosol is passed through a nozzle and directed against a flat plate called an impaction plate (see Figure 1.1a). Particles with sufficient inertia will cross the air streamlines and impact on the impaction surface. Particles with less inertia will stay in the streamlines and follow the airflow away from the impaction area. Impactors have been widely

used since their origin in 1860 (Marple 2004) and many commercial versions are available today.

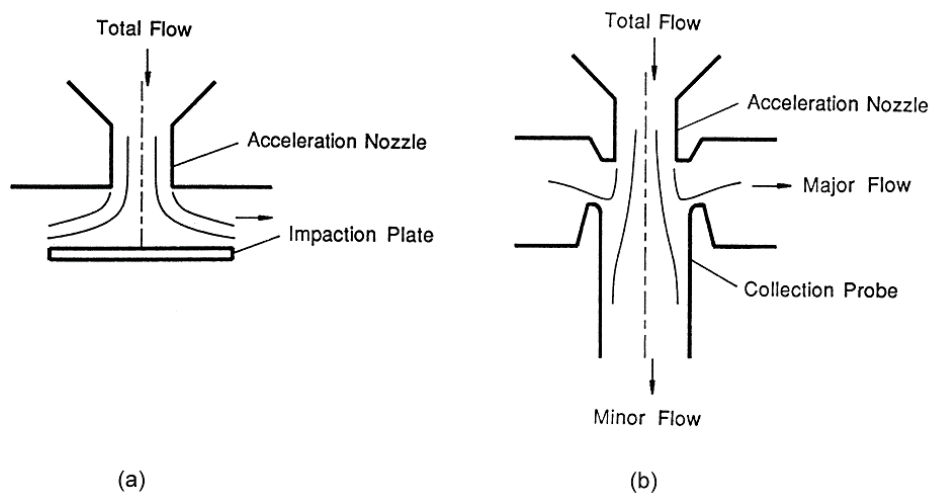


Figure 1. 1 inertial impactors: (a) plate impactor,
(b) virtual impactor (Marple, 2004).

More recently, virtual impactors have been developed. In a virtual impactor a receiving tube replaces the flat impaction plate as shown in Figure 1.1b. A small flow is passed through the receiving tube so that particles with sufficient inertia, that would have impacted the impaction plate of a conventional impactor, are thrown into the receiving tube. Particles above and below this cut-off size remain in air. These airborne particles can then be transported to another instrument.

A cyclone is another instrument that classifies by particle inertia; however, this inertia is generated by a centrifugal force. Cyclones do not have a sharp cut-off size, but they are able to collect much larger quantities of particles.

A centrifuge can also be used to increase the force field and is similar to having a greater gravitational force. The first aerosol centrifuge was called a

conifuge and was designed and produced by Sawyer and Walton (1950). The instrument consists of two metal cones fastened rigidly together with a conical gap between them (see Figure 1.2). These cones are connected to a high speed electric motor and spun along their axis. A pump draws air into the instrument from the top and passes it through the gap between the cones. Since the whole unit is rotating, particles are deposited around the outer cone. The position of the particles is a function of their aerodynamic diameter. This conifuge theory was later formulated by Stober and Zessack (1966).

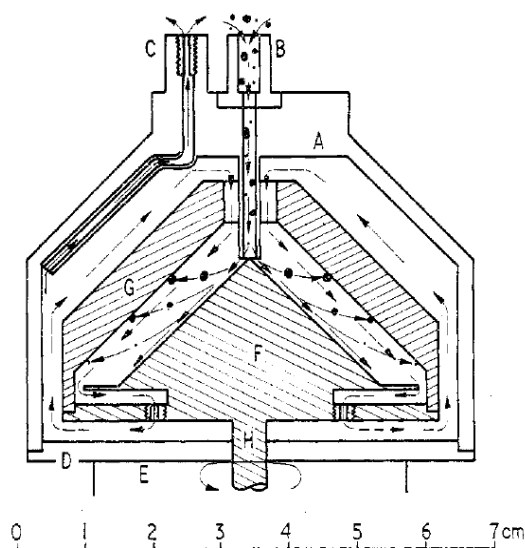


Figure 1. 2 conifuge (Poynting, 1972).

Another aerosol centrifuge that was designed and produced was called the Goetz Aerosol Spectrometer (Goetz, 1957). This instrument consists of two independent helical channels, where the outer envelope of the threads represents a cone with a solid angle of 3° (see Figure 1.3). A motor is used to spin the helicals and produces high centrifugal acceleration (ca. 20000 g). The floor, where the particles deposit, consists of a thin, removable foil that covered the inner surface of the outer cone. The location of particle deposition was correlated to the

aerodynamic particle size. The theoretical analysis of this centrifuge was studied by Preining (1962) and Stober and Zessack (1966).

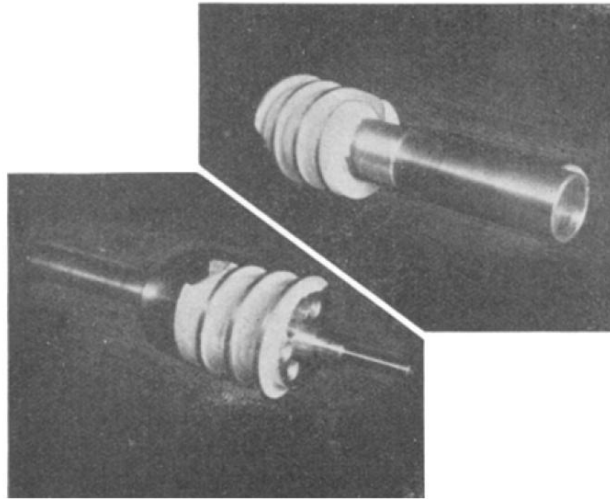


Figure 1.3 Helical shaped channel of Goetz aerosol spectrometer (Goetz, 1957).

Stöber and Flachsbart (1969) developed a Spinning Spiral Duct. Various modifications to this device have been studied (Hochrainer 1971; Moss et al. 1972; Kotrappa and Light 1972; Tillery 1974; Stöber 1975). Kotrappa and Light (1972) developed an instrument called the lovelace aerosol and particle separator (LAPS), as shown in Figure 1.4. The centrifuge spins at a high rotational speed and a particle-free sheath flow is introduced and travels through the centrifuge duct. Aerosol flow enters from a slit at the beginning of the duct's inner wall. Particles in the duct experience a centrifugal force when it is rotating causing them to deposit on the outer duct wall. The site of the deposition depends on the particle aerodynamic diameter. Large particles deposit quickly on the wall, while small ones continue with the flow and deposit further down. Asgharian and Godo (1999) theoretically investigated the air flow field in the centrifuge to predict the deposition length.

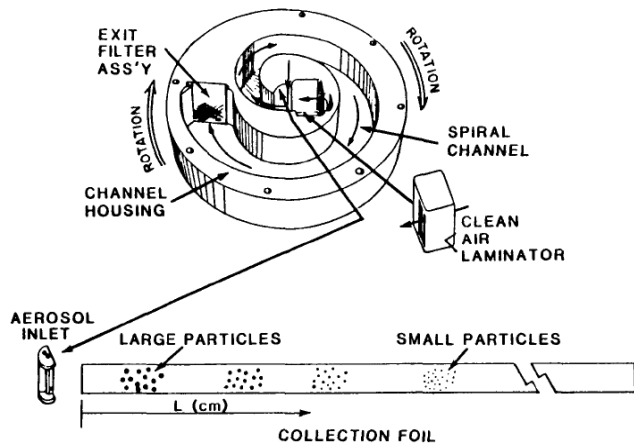


Figure 1. 4 schematic of the Aerosol and Particle Separator, LAPS (Cheng et al, 1988).

1.3 Monodisperse classifiers

Aerosol classifiers are used to produce a monodisperse aerosol, that is, they select a narrow range of particles from a larger distribution. These devices are used for many applications including: nano-particle generation, measuring particle count distributions, measuring particle properties and measuring the deposition of particles in filters and other devices.

1.3.1 Differential mobility analyzer

The force of gravity is often too weak for small (nano) particle deposition. Optical measurements of ultrafine particles, usually refers to particles smaller than 100 nm, are also difficult to characterize because of weak light scattering. To use impactors for nano-particle classification the pressure should be below atmospheric pressure, which risks volatile components being lost. One practical method to measure ultrafine particles is to use an electrostatic force. Charged particles move in an electric field with a velocity that depends on the particle size and the number of elementary charges on the particle. In the charging process,

large particles obtain multiple charges; however, small particles have a relatively high probability of having only one charge or remaining uncharged.

The differential mobility analyzer (DMA) uses this electrostatic force to classify particles and was designed by Knutson and Whitby (1975). It is currently used to produce a monodispersed aerosol for instrument calibration and particle sizing. However this process requires charge correction as the particles can have a different number of charges and sizes yet have the same electrical mobility. Therefore an inversion function is always required for calibrations or measurements using the DMA. If the charge distribution for all of the particle sizes is known, the particle size distribution can be determined from the electrical mobility distribution using the proper data inversion algorithms.

DMAs have been built with a variety of geometries. The most common geometry is the cylindrical DMA (cDMA) in which particle classification occurs between concentric cylinders as shown in Figure 1.5. A small aerosol flow is introduced through a slot on the outer cylinder and a larger, particle-free sheath flow is introduced at the top of the classifier. As the aerosol and the sheath flow carry through the channel, a voltage difference between the cylinders force charged particles to migrate across the channel. Only particles that are within a narrow range of electrical motilities will make it to the downstream port of the inner cylinder and be extracted.

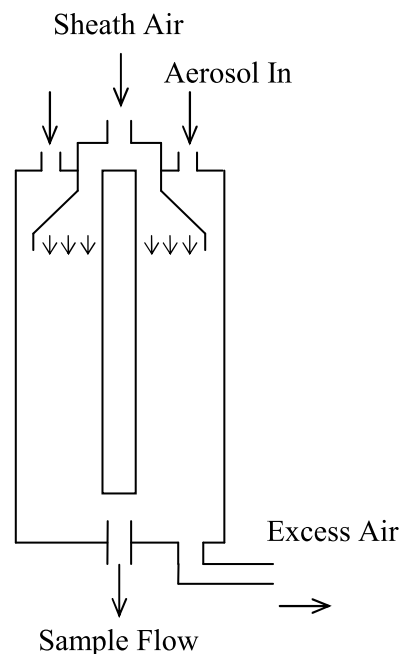


Figure 1. 5 Schematic of DMA.

Other instruments that use the electrical mobility method and have been commercialized are the Whitby Aerosol Analyzer (WAA) (Whitby et al. 1966), electrical aerosol analyzer (EAA) by Liu et al. (1974) and differential electrical mobility classifier (DEMC) of Erikson (1921). These classifiers combined with a detector can be used to measure the particle mobility size distribution. However at ambient concentrations the low level of aerosol charge concentration is hard to detect with an electrometer. This problem was overcome by the introduction of the continuous-flow, single particle-counting condensation particle counter (CPC; Agarwal and Sem 1978). By combining a DMA and CPC in series, while stepping through the DMA voltages, particle size distribution measurements are possible with the proper data inversion. This technique was commercialized by TSI and called the Differential Mobility Particle Sizer (DMPS).

However, the stepping process for DMPS was slow for some applications. Wang and Flagan (1990) showed that the particles can still be separated when the

electric field of the DMA is ramped continuously and the classified particles are counted in a real-time. This system was called the scanning electrical mobility spectrometer (SEMS) and later, with some modifications, TSI commercialized it as the Scanning Mobility Particle Sizer (SMPS).

1.3.2 Aerosol particle mass analyzer

The aerosol particle mass analyzer (APM) classifies aerosol particles according to their mass-to-charge ratio, by balancing centrifugal and electrostatic forces (Ehara et al. 1996). Figure 1.6 shows the cross section of the instrument. The APM consists of two rotating coaxial electrodes rotating at an equal angular velocity.

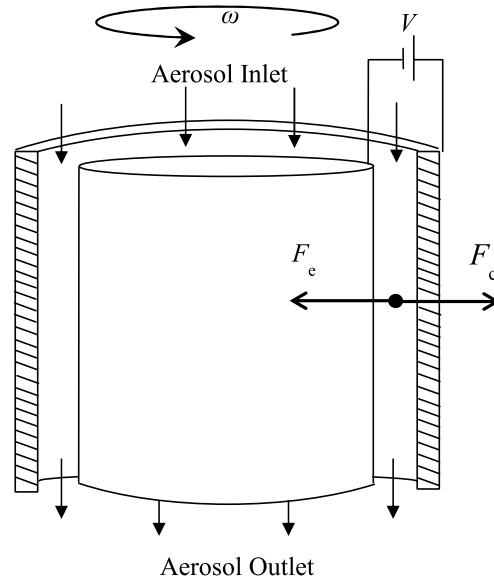


Figure 1. 6 Schematic of APM, aerosol particle mass analyzer.

As shown in the figure, a centrifugal (F_c) and an electrostatic force (F_e) act in opposite directions on each charged particle. When these two forces are

balanced, the particle pass through the classifier. Particles with mass-to-charge ratios greater than the balanced setpoint travel to the outer cylinder, while particles with mass-to-charge ratios less than the balanced setpoint travel to the inner cylinder, where they adhere due to van der Waal forces.

1.3.3 Couette CPMA

Particle losses in the APM have been found to be high under certain operating conditions (Olfert and Collings, 2005). Therefore, two new ideas for mass classification were conceived by Reavell and Rushton (2004): a Couette centrifugal particle mass analyzer (Couette CPMA) and Fluted CPMA. A Couette CPMA was examined (Olfert and Collings 2005, Olfert et al., 2006) and found to have better performance characteristics than the APM and Fluted CPMA. Also, the experimental performance results of the Couette CPMA closely matched the theoretical study (Olfert et al., 2006).

The Couette CPMA operation is similar to the APM, except that the inner cylinder of the Couette CPMA rotates slightly faster than the outer cylinder. This difference generates a stable system of forces and causes particles with the correct mass-to-charge ratio to converge to the equilibrium radius. The equilibrium radius is where the centrifugal force and the electrostatic forces are in balance. However particles with the correct mass-to-charge ratio are only classified by the APM if they start at the equilibrium radius. Due to this difference the Couette CPMA transfer function is more efficient than the APM and particle losses are reduced (Olfert and Collings, 2005).

1.4 Overview

Although there are several methods to measure the aerodynamic diameter of a particle, there has been little success in developing a practical instrument that

produces a monodisperse aerosol classified by aerodynamic diameter. A combination of a virtual impactor and a standard impactor has been used to produce relatively broad aerodynamically-classified distributions (Chein and Lundgren 1993). It has also been suggested that a monodisperse aerosol could be generated using an opposed migration aerosol classifier (OMAC) using a centrifugal force rather than an electrostatic force (Flagan, 2004) or by using an aerodynamic lens with a sheath flow (Kiesler and Kruis, 2012). This thesis reports the theoretical models of a new instrument, called the aerodynamic aerosol classifier (AAC), which produces a monodisperse aerosol based on particle aerodynamic diameter. The AAC produces a true monodispersed aerosol as it does not rely on particle charging and therefore does not classify multiply-charged particles like the DMA, CPMA, or APM. Two diffusion models and two non-diffusion models have been used to predict the performance of the AAC. The limiting trajectory and particle streamline models are analytical methods that do not include particle diffusion. To demonstrate the diffusion effect, a convective diffusion model has been developed by using the convective-diffusion equation for the AAC and solving it using the Crank-Nicolson method. The diffusing particle streamline model was also used and is an analytical model which approximates particle diffusion as a Gaussian cross-stream profile about the corresponding non-diffusing particle streamline. All of these theoretical models show the instrument has good classification properties for most aerosol applications including a relatively wide classification range, high resolution, and high penetration efficiency. The AAC can also be combined in series with a DMA to measure other important particle properties including: volume equivalent diameter, effective density, shape factor and mass. In chapter 4, the aforementioned properties of soot particles were calculated from the aerodynamic

diameter and mobility diameter of soot particles produced from an inverted burner.

References

- Agarwal, J. K., and Sem, G. J. (1978). Generating submicron monodisperse aerosol for instrument calibration. *TSI Quarterly*, pp. 3–8.
- Asgharian, B. and Godo, M. N. (1999). Size separation of spherical particles and fibers in an aerosol centrifuge. *Aerosol Science and Technology*, 30, 383-400.
- Baron P. A. and Willeke K., (2001). Aerosol Measurement - Principles, Techniques, and Applications -2nd Edition, *John Wiley & Sons*, ISBN 0-471-35636-0.
- Chein, H., and Lundgren, D. A. (1993). Virtual impactor with clean air core for the generation of aerosols with narrow size distributions. *Aerosol Science and Technology*, 18, pp. 376–388.
- Cheng, Y.-S., Yeh, H. C., and Allen M. D. (1988). Physical Characterisation and Aerodynamic Behaviour of Plate-Like Particles, *The Annals of Occupational Hygiene* (32), pp. 369-378.
- Ehara, K., Hagwood, C., and Coakley, K. J. (1996). Novel method to classify aerosol particles according to their mass-to-charge ratio – aerosol particle mass analyser. *Journal of Aerosol Science*, 27(2):217–234.
- Erikson, H. A. (1921). The change of mobility of the positive ions in air with age. *Phys. Rev.* 18:100–101.

-
- Flagan, R.C. (2004). Opposed migration aerosol classifier (OMAC). *Aerosol Science and Technology*, 38, pp. 890–899.
- Goetz, A. (1957). An instrument for the quantitative separation and size classification of airborne particulate matter down to 0.2 micron, *Geophys. pura appl.*, 36 pp. 49–69.
- Hochrainer, D. (1971). A New Centrifuge to Measure the Aerodynamic Diameter of Aerosol Particles in the Submicron Range, *J. Colloid Interface Sci.* 36:191–194.
- Kiesler, D. and Kruis, F.E., (2012). Feasibility study of a Differential Aerodynamic Diameter Analyzer, European Aerosol Conference, Granada, Spain.
- Knutson, E. O., and Whitby, K. T. (1975). Aerosol classification by electric mobility: Apparatus, theory, and applications. *Journal of Aerosol Science*, 6:443–451.
- Kotrappa, P., and Light, M. E. (1972). Design and Performance of the Lovelace Aerosol and Particle Separator, *Rev. Sci. Instrum.* 43:1106–1112.
- Kulkarni P., Baron P. A., Willeke K., (2011). Aerosol Measurement - Principles, Techniques, and Applications -3rd Edition, *John Wiley & Sons*, ISBN: 9780470387412.
- Liu, B. Y. H., Whitby, K. T., and Pui, D. Y. H. (1974). A portable electrical analyzer for size distribution measurement of submicron aerosols. *Journal of the Air Pollution Control Association*, 24:1067–1072.
- Marple V.A. (2004). History of impactors-the first 110 years, *Aerosol Science and Technology*, 38, pp. 247–292.

-
- Moss, O. R., Ettinger, H. J., and Coulter, J. R. (1972). Aerosol Density Measurements Using a Modified Spiral Centrifuge Aerosol Spectrometer, *Environmental Science & Technology*, 6:614–617.
- Olfert, J. and Collings, N., (2005). New method for particle mass classification — The Couette centrifugal particle mass analyzer, *Journal of Aerosol Science*, vol. 36, pp. 1338–1352.
- Olfert, J.S., Reavell, K.StJ., Rushton, M.G., Collings, N. (2006). The experimental transfer function of the Couette centrifugal particle mass analyzer, *Journal of Aerosol Science*, 37 (12), pp. 1840-1852.
- Poynting, R (1972), A miniature conifuge, *Journal of Physics E: Scientific Instruments*,(5) pp. 52-55.
- Preining, O. (1962). The Goetz Aerosol Spectrometer. Problems of operation and evaluation, *Staub*, 22, pp. 129–133.
- Reavell, K. and Rushton, M. (2004). U.K Patent.
- Sawyer, K.F., Walton, W.H. (1950) The 'Conifuge' - A Size-separating Sampling Device for Airborne Particles, *Journal of Scientific Instruments*, 27 p. 272.
- Spurny K. R. (1998): Methods of Aerosol Measurement before the 1960s, *Aerosol Science and Technology*, 29:4, 329-349.
- Stöber, W., and Flachsbart, H. (1969). Size Separating Precipitation of Aerosols in a Spinning Spiral Duct, *Environmental Science & Technology*. 3:1280–1296.
- Stöber W., Zessack U., Zentralbl. (1966), *biol. Aerosolforsch.*, 13 p. 263.

-
- Stöber, W. (1975). Design, Performance and Application of Spiral Duct Centrifuges. In *Fine Particles* edited by B. Y.H. Liu. Academic Press, New York, p. 351.
- Tillery, M. I. (1974). A Concentric Aerosol Spectrometer, *American Industrial Hygiene Association Journal*. 35:62–74.
- Wang, S. C., and Flagan, R. C. (1990). Scanning electrical mobility spectrometer, *Aerosol Science and Technology*, 13:230–240.
- Whitby, K. T., and Clark, W. E. (1966). Electrical aerosol particle counting and size distribution measuring system for the 0.015 to 1 μm size range. *Tellus* 18:573–586.

Chapter 2

Theoretical Models of the Aerodynamic

Aerosol Classifier ¹

In this chapter the principles of the aerodynamic aerosol classifier (AAC) will be presented. Four theoretical models describe the transfer function of the instrument. Analytical particle streamline models (with and without the effects of particle diffusion), like those often used for mobility classifiers, are developed for the case when the centrifugal acceleration field is assumed to be uniform in the radial direction. More accurate models are developed when this assumption is not made. These models are the analytical limiting trajectory model which neglects the effects of diffusion and a numerical convective diffusion model that does not. It is shown that these models agree quite well when the gap between the cylinders

¹ The content of this chapter is published in:

F. Tavakoli & J. S. Olfert (2013): An Instrument for the Classification of Aerosols by Particle Relaxation Time: Theoretical Models of the Aerodynamic Aerosol Classifier, *Aerosol Science and Technology*, 47:8, 916-926.

is small compared to the radii of the cylinders. The models show that, theoretically, the AAC has a relatively wide classification range and high resolution.

2.1 Working principle

The particle relaxation time is defined as the particle's mobility (B) multiplied by its mass (m) (Hinds, 1999). The aerodynamic diameter can be related to the particle relaxation time, τ , by assuming that the particle is spherical with standard density (i.e. the assumptions made in defining the aerodynamic equivalent diameter),

$$\tau \equiv Bm = \frac{C_c(d_{ae})\rho_0 d_{ae}^2}{18\mu} \quad (2.1)$$

where μ is the viscosity of the gas, C_c is the Cunningham slip correction factor, and d_{ae} is the aerodynamic diameter of the particle (see Appendix A).

As shown in Figure 2.1 the AAC consists of two concentric cylinders rotating in the same direction and at the same rotational speed². The particles, carried along by the aerosol flow, Q_a , enter the gap between the two cylinders through a slit in the inner cylinder wall. A sheath flow of particle-free air, Q_{sh} , is also introduced between the two cylinders. In the absence of rotation the particles will travel between the inner cylinder wall and the aerosol streamline, as shown in Figure 2.2. However, when the cylinders are rotated, the particles experience a centrifugal force and drag force in the radial direction. The particles are also carried in the axial direction by the flow of the sheath and aerosol flows. The

² A separate embodiment could employ cylinders rotating at different rotational speeds but that is not investigated here.

radial forces cause the particles to move toward the outer cylinder and particles of a narrow range of particle relaxation times exit with the sample flow. Particles with larger relaxation times impact and adhere to the outer cylinder and particles with smaller relaxation times exit the classifier with the exhaust flow. Models describing the classification of these particles by particle relaxation time are described below.

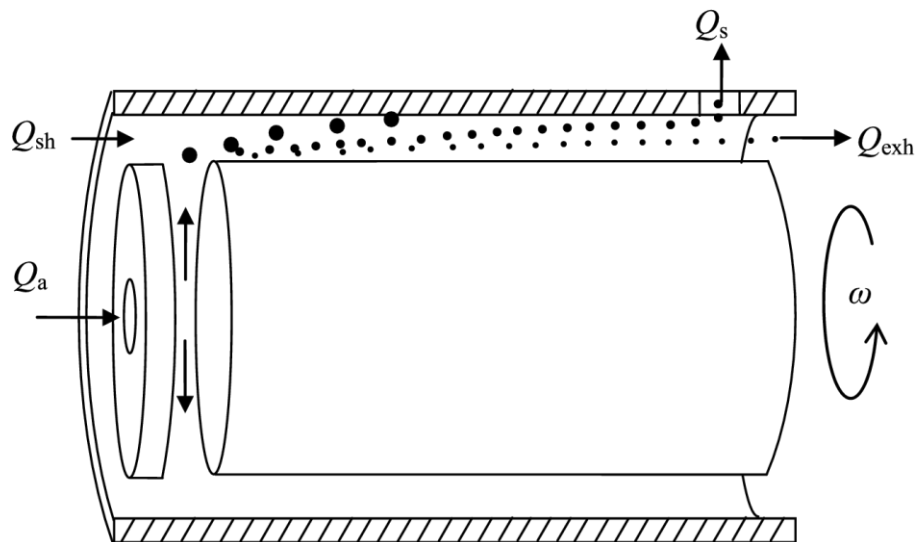


Figure 2. 1 Schematic of the Aerodynamic Aerosol Classifier.

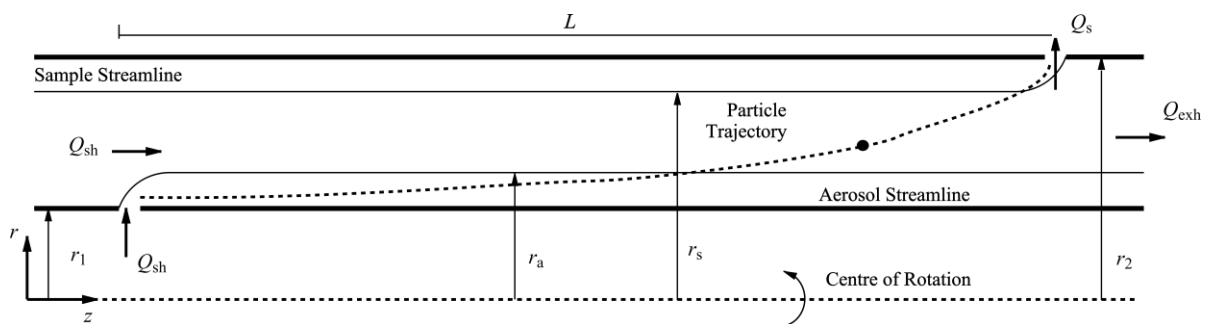


Figure 2. 2 Details of the particle trajectory and flows between the cylinders.

2.2 Non-diffusion models

2.2.1 Limiting trajectory model

The velocity of the particles in the classification region of the instrument (Figure 2.2) can be derived by Newton's second law using a non-inertial reference frame, in absence of space charge. In the radial direction, the friction force, which is given by Stokes law (v_r/B , where v_r is the velocity of particle with respect to the fluid and B is mechanical mobility), will be equal to the centrifugal force.³ Therefore, the particle's velocity in the radial direction, v_r , will be,

$$v_r = \frac{dr}{dt} = Bm\omega^2 r = \tau\omega^2 r \quad (2.2)$$

where r is the radial position of the particle with respect to the axis of rotation, ω is the rotational speed of the cylinders, m is the mass of the particle, and τ is the particle relaxation time. The particle velocity in the axial direction, v_z , will simply be equal to the velocity of the carrier gas in the axial direction, u , assuming the time particle velocity reach to u is small with respect to classification time,

$$v_z = \frac{dz}{dt} = u. \quad (2.3)$$

The velocity profile is assumed to be uniform (i.e., u is constant). As will be shown in the diffusion model, this assumption has no effect on the calculated instrument transfer function compared to a varying fluid velocity (as was also shown in the derivation of the transfer function of the DMA by Knutson and

³ In an inertial reference frame it would be said that the friction force will be equal to the mass of the particle multiplied by the acceleration of the particle in the radial direction, where the acceleration is $\omega^2 r$.

Whitby (1975), Hoppel, (1978)). Fluid flow in this instrument is also assumed to be laminar. Meseguer and Marques (2002) studied flow instability between two rotating coaxial cylinders with an imposed axial pressure gradient (spiral Poiseuille flow). They have shown that for rigid-body rotation the flow is stable for all rotational speeds if the axial Reynolds number is lower than a critical value. Typical axial flows in the AAC will be relatively low and are far below the critical value given by Meseguer and Marques (2002).

Using the chain rule and differentiating, the radial position of the particle can be found as a function of the axial position,

$$r(z) = r_{\text{in}} \exp\left(\frac{\tau\omega^2 z}{u}\right), \quad (2.4)$$

where r_{in} is the initial position of the particle when it enters the classifier, which will be between r_1 and r_a .

The instrument transfer function is defined as the probability that an aerosol particle that enters the aerosol inlet with relaxation time, τ , will exit with the sampling flow. The transfer function can be found by determining the limiting trajectory of the particles in a similar method as was done by Wang and Flagan (1990) for the DMA.

The largest particle (i.e., the largest τ) that will pass through the classifier, exiting the classifier in the sample flow, Q_s , will start at $r_{\text{in}} = r_1$ and will reach r_2 at the end of the classifier ($z = L$). Therefore, from Equation 2.4,

$$\tau_{\text{max}} = u \frac{\ln(r_2/r_1)}{\omega^2 L} = \frac{(Q_{\text{sh}} + Q_a) \ln(r_2/r_1)}{\pi(r_2^2 - r_1^2)} \frac{1}{\omega^2 L}. \quad (2.5)$$

The smallest particle that will be classified, τ_{\min} , will enter the classifier at $r_{\text{in}} = r_a$ and will reach r_s at the end of the classifier. The radii r_a and r_s can be related to the radii r_1 and r_2 , realizing that for uniform flow,

$$u = \frac{Q_{\text{sh}} + Q_a}{\pi(r_2^2 - r_1^2)} = \frac{Q_{\text{sh}}}{\pi(r_2^2 - r_a^2)} = \frac{Q_s}{\pi(r_2^2 - r_s^2)}. \quad (2.6)$$

Therefore,

$$\begin{aligned} \tau_{\min} \\ = \frac{(Q_{\text{sh}} + Q_a)}{2\pi\omega^2 L(r_2^2 - r_1^2)} \ln \left(\frac{Q_{\text{sh}} + Q_a - Q_s(1 - r_1^2/r_2^2)}{Q_{\text{sh}} + Q_a - Q_{\text{sh}}(1 - r_1^2/r_2^2)} \right). \end{aligned} \quad (2.7)$$

Particles with $\tau > \tau_{\max}$ will intercept the outer cylinder wall before reaching the exit slit and will adhere to the cylinder surface, while particles with $\tau < \tau_{\min}$ will flow past the exit slit and be carried out of the instrument with the exhaust flow.

The transfer function is determined by calculating the probability that an aerosol particle that enters the aerosol inlet will exit with the sample flow. To be classified, a particle must migrate into the sample flow, defined by the sample streamline ($r_s \leq r < r_2$), by the time the particle has reached the end of the classifier ($z=L$). For particles with relaxation times greater than τ_{\max} or less than τ_{\min} , the probability they will exit with the sample flow is zero. For particles with relaxation times between τ_{\max} and τ_{\min} , only a fraction will be classified. For particles with relaxation times greater than τ_{\min} , only particles with an initial radial position between the aerosol streamline, r_a , and a critical initial position, r_c , will be classified. The trajectory of a particle with initial position r_c is defined as the limiting trajectory: particles with initial position $r_c < r_{\text{in}} < r_a$ will be classified

and particles with initial position $r_{in} < r_c$ will not. It is assumed that particles entering the classifier will be uniformly distributed between the inner radius and the aerosol streamline ($r_1 < r_{in} < r_a$). Therefore, the probability that the aerosol will be classified is simply the fraction (f) of the aerosol flow that enters between the critical radius and the aerosol streamline,

$$f_1 = \frac{r_a^2 - r_c^2}{r_a^2 - r_1^2}. \quad (2.8)$$

The limiting trajectory for $\tau > \tau_{min}$ will be the particle that starts at r_c and reaches r_s . Substituting this condition ($r_{in} = r_c$ and $r(L) = r_s$) into Eq. 2.4 and solving for the aerosol fraction that is classified, f_1 , reveals,

$$f_1 = \frac{Q_{sh} + Q_a - \exp\left(\frac{-2\tau\omega^2 L\pi(r_2^2 - r_1^2)}{Q_{sh} + Q_a}\right) (Q_{sh} + Q_a - Q_s(1 - r_1^2/r_2^2))}{Q_a(1 - r_1^2/r_2^2)} - \frac{Q_{sh}}{Q_a}. \quad (2.9)$$

Likewise, for particles with $\tau < \tau_{max}$, the particles starting at the critical radius, r_c , must reach r_2 by the end of the classifier. The fraction f_2 is the aerosol fraction with $\tau < \tau_{max}$ that enters between r_c and r_1 and exits the classifier in the sample flow,

$$f_2 = \frac{r_c^2 - r_1^2}{r_a^2 - r_1^2}. \quad (2.10)$$

Substituting $r_{in} = r_c$ and $r(L) = r_2$ into Equation 2.4 and solving for the aerosol fraction, f_2 , gives,

$$f_2 = \frac{Q_{sh} + Q_a}{Q_a} \left(1 - \frac{1 - \exp\left(\frac{-2\tau\omega^2 L\pi(r_2^2 - r_1^2)}{Q_{sh} + Q_a}\right)}{1 - r_1^2/r_2^2} \right). \quad (2.11)$$

Furthermore, if the sample flow rate is smaller than the aerosol flow rate, then the transfer function cannot be larger than, $f_3 = Q_s/Q_a$. The transfer function, Ω , will be the minimum of these three fractions or one. Therefore, the transfer function can be expressed as, $\Omega = \max[0, \min(f_1, f_2, f_3, 1)]$.

2.2.2 Particle streamline model

Knutson and Whitby (1975) proposed a mathematical model using a stream function, ψ , and defining an electric flux function, ϕ to derive the DMA transfer function. When the flow is axisymmetric, laminar, and incompressible ($\nabla \cdot \mathbf{v} = 0$), the stream function can be defined as

$$\psi(r, z) = \int^{r,z} [r u_r dz - r u_z dr]. \quad (2.12)$$

Similarly, the DMA electric flux function, ϕ , can be defined because $\nabla \cdot \mathbf{E} = 0$, where \mathbf{E} is the electrostatic field. In the AAC a centrifugal acceleration field, \mathbf{a} , is used to classify the particles where the acceleration in the radial direction is $a_r = \omega^2 r$ and there are no acceleration in the axial and azimuthal direction ($a_z = a_\theta = 0$). This acceleration field is not a solenoidal vector field ($\nabla \cdot \mathbf{a} \neq 0$). However, if the gap between the two cylinders, h , is small compared to the mean radius of the cylinders, $\bar{r} = (r_1 + r_2)/2$, in other words, when $\tilde{h} \equiv \frac{h}{\bar{r}}$ is small, then the acceleration field can be assumed to be constant in the gap, and the acceleration field will approximately be solenoidal. Under these approximations ϕ can be defined as,

$$\phi(r, z) = \int^{r,z} [r a_r dz - r a_z dr]. \quad (2.13)$$

Integrating Equation 2.13, the change in ϕ from the aerosol inlet to the outlet is:

$$\Delta\phi = \bar{r}^2 \omega^2 L. \quad (2.14)$$

Following Knutson and Whitby (1975) and Stolzenburg (1988) the non-diffusing transfer function Ω_{nd} is obtained and the non-dimensional form can be expressed as,

$$\begin{aligned} \Omega_{nd}(\tilde{\tau}, \beta, \delta) = & \frac{1}{2\beta(1-\delta)} [|\tilde{\tau} - (1 - \beta)| + \\ & |\tilde{\tau} - (1 - \beta)| - |\tilde{\tau} - (1 + \beta\delta)| - |\tilde{\tau} - (1 - \beta\delta)|], \end{aligned} \quad (2.15)$$

where β and δ are dimensionless flow parameters expressed as,

$$\beta = \frac{Q_s + Q_a}{Q_{sh} + Q_{exh}}, \quad (2.16)$$

$$\delta = \frac{Q_s - Q_a}{Q_s + Q_a}, \quad (2.17)$$

and the dimensionless particle relaxation time is defined as

$$\tilde{\tau} = \frac{\tau}{\tau^*}. \quad (2.18)$$

The value τ^* is the particle relaxation time at the maximum of the transfer function and is defined as, $\tau^* = (\tau_{max} + \tau_{min})/2$. In the particle streamline model, this value (τ_{ps}^*) can be found from,

$$\tau_{PS}^* = \frac{Q_{sh} + Q_{exh}}{\pi\omega^2(r_1 + r_2)^2L}. \quad (2.19)$$

2.2.3 Discussion of non-diffusion models

Figure 2.3 shows the normalized non-diffusion transfer function with balanced flows ($Q_{sh}=Q_{exh}$ and $Q_a=Q_s$; or $\delta = 0$) and aerosol to sheath flow ratio of 0.1 ($\beta=0.1$) for the particle streamline model and the limiting trajectory model for two values of \tilde{h} . One of the values of \tilde{h} represents the proposed dimensions of the AAC shown in Table 2.1. For this case, \tilde{h} is relatively small (the gap is relatively small with respect to the cylinders' radii) with a value of 0.0455. The other case shows an example when the gap is ten times larger than the proposed dimensions and all other dimensions are the same ($\tilde{h}=0.455$). In this figure τ is normalized with respect to τ^* for each respective model (i.e. $\tilde{\tau} = \tau/\tau_{LT}^*$ or $\tilde{\tau} = \tau/\tau_{PS}^*$).

Table 2.1. Proposed dimensions and operating conditions.

Property	Value
r_2 (mm)	45
r_1 (mm)	43
L (mm)	210
Q_{sh} (L/min)	3
$Q_a = Q_s$ (L/min)	0.3
Temperature ($^{\circ}$ C)	20
Pressure (atm)	1

Recall that the particle streamline model assumes the centrifugal force between the cylinders is constant and it neglects the divergence of the centrifugal acceleration field. This model is a simplification of the actual classification in the AAC, which is better represented with the limiting trajectory model. As shown in the figure, the particle streamline model closely approximates the limiting

trajectory model when \tilde{h} is small, but it is a poor approximation when \tilde{h} is large. For small values of \tilde{h} the width of the transfer function (τ_{\max} and τ_{\min}) between the two models are very similar and the particle streamline model slightly overestimates the amplitude of the transfer function ($\Omega_{LT}(\tau_{LT}^*) = 0.96 \Omega_{PS}(\tau_{PS}^*)$). For large values of \tilde{h} the difference between the widths of the transfer functions become apparent and the particle streamline model greatly overestimates the amplitude of the transfer function ($\Omega_{LT}(\tau_{LT}^*) = 0.72 \Omega_{PS}(\tau_{PS}^*)$). It should also be noted (because it cannot be seen in the figure) that there is also a very small difference in the location of the peak of the transfer functions (τ^*) between the two models. For $\tilde{h} = 0.0455$ the difference between τ_{PS}^* and τ_{LT}^* is 0.007% and for $\tilde{h} = 0.455$ the difference between τ_{PS}^* and τ_{LT}^* is 0.7%. This small difference suggests that it is reasonable to approximate the centrifugal force as a constant using the value of the force at r_c .

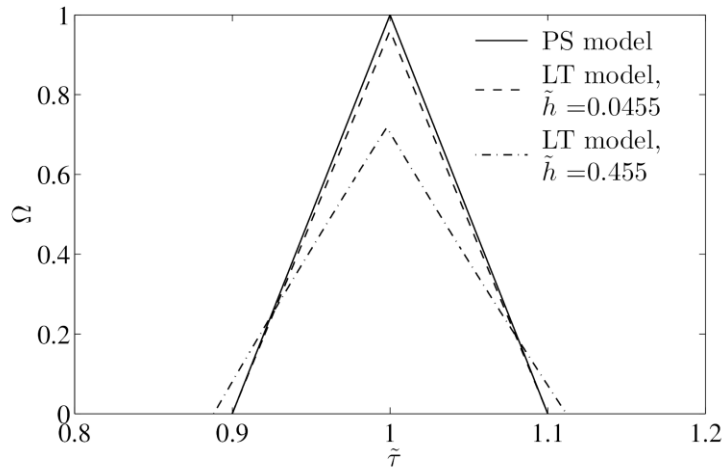
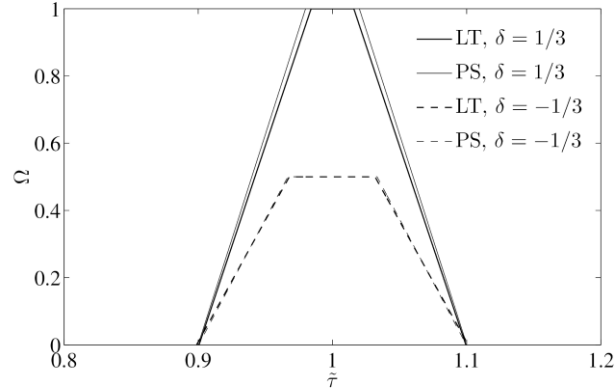


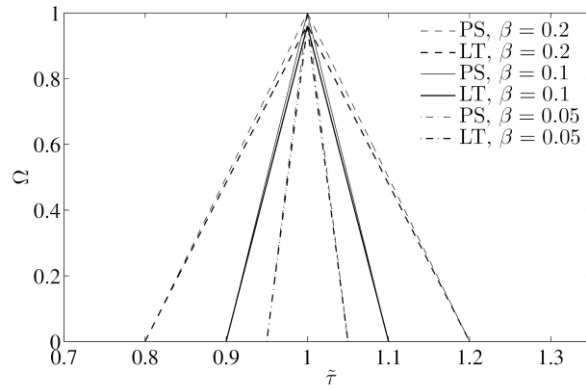
Figure 2. 3 AAC transfer function for two non-diffusion models with balanced flows ($\delta=0$) and aerosol to sheath flow ratio of 0.1 ($\beta=0.1$). The solid line shows the particle streamline model, and dashed and dashed-dot lines represent the limiting trajectory model.

From Figure 2.3 it is apparent that the largest difference between the models is the amplitude of the transfer functions. The maximum amplitude of the particle streamline model will always be 1 when using balanced flows because this model assumes that the centrifugal acceleration field does not diverge (it is analogous to the work of Stolzenberg (1988) who showed that the electric flux function in the DMA does not diverge, $\nabla \cdot \mathbf{E} = 0$). However, in reality the centrifugal force used in the AAC causes the particles to diverge and the radial distance between the particles increases as the particles move in the axial direction. This causes particles with relaxation time τ^* that enter the classification region near $r=r_a$ to impact the outer cylinder and those that enter near $r=r_1$ will exit the classifier in the exhaust flow, resulting in a transfer function less than 1. However, as \tilde{h} becomes small this effect becomes negligible and the maximum amplitude of the transfer function approaches 1.

Like the DMA, it is expected that the AAC would normally be operated with balanced flows and at an aerosol to sheath flow ratio of 0.1 as shown in Figure 2.3. Figure 2.4 shows examples of the transfer function where the flows are not balanced (Figure 2.4a) or where the aerosol to sheath flow ratio varied (Figure 2.4b) for the proposed geometry in Table 2.1. Like the DMA, using unbalanced flows results in trapezoidal transfer functions and using lower aerosol to sheath flow ratios (smaller β) results in higher resolution. As before the two models in these cases agree very well.



(a)



(b)

Figure 2. 4 Transfer function of the AAC using the limiting trajectory model (thick lines) and particle streamline model (thin lines) for (a) unbalanced flows ($\delta \neq 0$) when $\beta = 0.1$ and (b) balanced flows ($\delta = 0$) at different aerosol to sheath flow ratios.

2.3 Diffusion models

The previous models of the AAC did not include particle diffusion. Therefore, two diffusion models have been developed to show the effect of diffusion on the transfer function of the AAC.

2.3.1 Convective diffusion model

Here, a Eulerian diffusion model has been used to model the diffusion effect in the AAC. The convective diffusion of particles can be modeled using the convective diffusion equation as given by Friedlander (2000). Olfert and Collings (2005) have used a similar model to show the diffusion effect in the APM and Couette CPMA. The convective diffusion equation for incompressible flow can be written as,

$$\frac{\partial n}{\partial t} + \mathbf{u} \cdot \nabla n = D \nabla^2 n - \nabla \cdot \mathbf{c}n, \quad (2.20)$$

where n is the particle concentration, \mathbf{u} is the gas velocity, \mathbf{c} is the particle migration velocity, and D is the diffusion coefficient, which can be calculated using the Stokes-Einstein equation ($D=kTB$, where k is Boltzmann's constant and T is the temperature). The particle migration velocity is the particle velocity, \mathbf{v} , relative to the fluid velocity, \mathbf{u} , so that $\mathbf{c} = \mathbf{v} - \mathbf{u}$. For the AAC the particle migration velocity will be equal to the particle velocity in the radial direction, $c_r = \tau\omega^2 r$ (see Equation 2.2).

The convection diffusion equation is rewritten for a two-dimensional fully developed flow. To simplify the analysis, diffusion in the z -direction is neglected, since it will be small compared to the diffusion term in the r -direction and the convection term in the z -direction. Therefore, the non-dimensional equation can be written for the two-dimensional space as,

$$\frac{\partial \tilde{n}}{\partial \tilde{z}} = \frac{1}{2} \eta^2 \frac{\partial^2 \tilde{n}}{\partial \tilde{r}^2} - \zeta \frac{\partial \tilde{n}}{\partial \tilde{r}}, \quad (2.21)$$

where $\tilde{z} = z/L$ and $\tilde{r} = r/\delta$ are non-dimensional lengths. $\tilde{n} = n/n_0$ is the non-dimensionalized particle concentration, where n_0 is the initial particle concentration in the aerosol flow. Flow velocity, $u(r)$, in the z -direction is considered parabolic. The dimensionless constant, η , is defined as the ratio of radial diffusion length to radial convection length,

$$\eta = \frac{\sqrt{2DL/u}}{h}, \quad (2.22)$$

where, h is the gap between two cylinders, $r_2 - r_1$. Another dimensionless constant, ζ , is defined as the ratio of the characteristic time for a particle to travel the length of the classifier to the characteristic time for it to travel the gap between the cylinders,

$$\zeta = \frac{\tau\omega^2 rL}{uh}. \quad (2.23)$$

Aerosol particles adhere to a wall surface due to the existence of London–van der Waals forces between particles and the surface (Friedlander, 2000). Hence, in aerosol science the concentration of particles at a wall is conventionally considered to be zero, which is usually an extremely good approximation for common aerosol particles and geometries⁴. Therefore, the initial and boundary conditions for this system will be:

⁴ There are some studies that suggest the particle concentration is proportional to the particle flux to the wall (Gallis et al., 2008); however, Tavakoli et al. (2011) showed that this boundary condition does not have any significant effect on aerosol transport in channels.

$$\tilde{n}(\tilde{r}, 0) = 1 \text{ for } \frac{r_1}{h} < \tilde{r} \leq \frac{r_a}{h} \quad (2.24)$$

$$\tilde{n}(\tilde{r}, 0) = 0 \text{ for } \frac{r_a}{h} < \tilde{r} < \frac{r_2}{h}$$

$$\tilde{n} = \tilde{n}(r_1/h, \tilde{z}) = \tilde{n}(r_2/h, \tilde{z}) = 0 \quad (2.25)$$

Equation (2.21) has been solved numerically using the Crank-Nicolson method (Smith, 1978). The Crank-Nicolson method is a finite difference method which is unconditionally stable for diffusion equations. This method converges faster than other implicit methods and has second-order accuracy in all dimensions (see Appendix D).

The value of the transfer function for a given relaxation time can be found by calculating the ratio of the flux of particles exiting with the sample flow to the flux of particles entering the classifier,

$$\Omega(\tau, \tau^*) = \frac{\int_{r_s}^{r_2} u(r)n(r, \tau)dr}{\int_{r_1}^{r_2} u(r)n(r, \tau)dr}. \quad (2.26)$$

The radial position of the sample streamline, r_s , can be calculated by solving the following equation:

$$Q_s = \int_{r_s}^{r_2} 2\pi r u(r) dr. \quad (2.27)$$

Equation 2.21 is solved repeatedly for different τ at a given τ^* to obtain the transfer function shape.

2.3.2 Diffusing particle streamline model

Assuming that the non-diffusing particle streamline model is a good approximation of the AAC transfer function (as discussed in Sections 3.2 and 3.3), a theoretical diffusion model based on the streamline model can be developed. Stolzenburg (1988) developed a particle streamline diffusion model for the DMA assuming that diffusion spreads particles in a Gaussian cross-stream profile about the corresponding non-diffusing particle streamline. The same method can be used here for the AAC and following the work of Stolzenburg (1988) and the derivation of the non-diffusion streamline model shown in Section 3.2, the diffusion transfer function, Ω_d can be given

$$\begin{aligned} \Omega_d(\tilde{\tau}, \beta, \delta, \sigma) = & \frac{\sigma}{\sqrt{2}\beta(1-\delta)} \left[\varepsilon\left(\frac{\tilde{\tau} - (1 + \beta)}{\sqrt{2}\sigma}\right) \right. \\ & + \varepsilon\left(\frac{\tilde{\tau} - (1 - \beta)}{\sqrt{2}\sigma}\right) - \varepsilon\left(\frac{\tilde{\tau} - (1 + \beta\delta)}{\sqrt{2}\sigma}\right) \\ & \left. - \varepsilon\left(\frac{\tilde{\tau} - (1 - \beta\delta)}{\sqrt{2}\sigma}\right) \right] \end{aligned} \quad (2.28)$$

where $\varepsilon(x) = x \cdot \text{erf}(x) + e^{-x^2}/\sqrt{\pi}$ and $\text{erf}(x)$ is the error function, and the standard derivation, σ , is given by

$$\sigma^2 = G_{\text{AAC}} \frac{4\pi LD}{Q_{\text{sh}} + Q_{\text{exh}}}. \quad (2.29)$$

G_{AAC} is a non-dimensional geometry factor (see Appendix B), it can be calculated from Stolzenburg (1988) and its value for the proposed geometry in Table 2.1 is 61.7. As discussed in Section 3.2 and 3.3 this method is only a good approximation when the gap between cylinders is considerably smaller than the mean of cylinders' radii.

2.3.3 Discussion of diffusion models

In the convective diffusion model Equation 2.21 shows that the solution only depends on two variables; η and ζ . In the convective diffusion model, η characterizes the effect of diffusion in the classifier and ζ determines the location of the transfer function. By assuming Q_a and $Q_s \ll Q_{sh}$, τ^* can be approximated using Equation 2.5 and 7, which results in,

$$\tau_{LT}^* \approx \frac{u}{\omega^2 L} \ln\left(\frac{r_2}{r_1}\right). \quad (2.30)$$

Adding the assumption $\tilde{h} \ll 1$ and using a first-order Taylor series expansion, τ^* is approximated by,

$$\tau_{LT}^* \approx \frac{uh}{\omega^2 \bar{r} L}. \quad (2.31)$$

Thus,

$$\zeta \approx \tilde{\tau}, \quad (2.32)$$

Also, using Equation 2.19 and assuming $\tilde{h} \ll 1$ gives $\tau_{LT}^* = \tau_{PS}^*$. Thus,

$$\tilde{\tau}_{LT} = \tilde{\tau}_{PS} = \zeta, \quad (2.33)$$

which shows how the convective diffusion model and non-diffusion models are linked.

In Equation 2.22 and Equation 2.29, η and σ characterizes the effect of diffusion for the convective diffusion model and diffusing particle streamline model; respectively. For balanced flows, when $\tilde{h} \ll 1$, from Equation 2.22 and 29 we have

$$\sigma = \eta \sqrt{\frac{G_{AAC} h}{2\bar{r}}}. \quad (2.34)$$

and for the proposed geometry $\sigma = 1.23 \eta$.

Figure 2.5 shows the transfer function for the AAC for the non-diffusion limiting trajectory model, the convective diffusion model for $\eta^* = 0$ and $\eta^* = 0.05$, and its corresponding value ($\sigma^* = 0.0616$) in the diffusing particle streamline model. The equivalent aerodynamic diameter for the diffusion models is 50 nm for the dimensions shown in Table 2.1. Here, η^* and σ^* is the η and σ value where $\tau = \tau^*$. As η^* and σ^* increases the diffusion effect increases which leads to a broader transfer function and greater diffusional losses. The effect of diffusion on resolution is more clearly seen in Figure 2.6, which shows the classifier resolution as a function of the dimensionless numbers η^* and σ^* from the convective diffusion model and diffusing particle streamline respectively; when $\delta=0$ and $\beta=0.1$. The resolution, R , is defined as $R=\tau^*/FWHM$, where FWHM is the full-width half maximum of the transfer function. If diffusional effects are neglected, \tilde{h} is small, and the flows are balanced, then $R = 1/\beta$. As shown above, the resolution decreases for smaller particle sizes (large η^* and σ^*) because of the diffusion effect; and the resolution for larger particles (small η^* and σ^*) asymptotically approaches the value of $1/\beta$. Also Figure 2.6 shows that the convective diffusion and the diffusing particle streamline models agree very well.

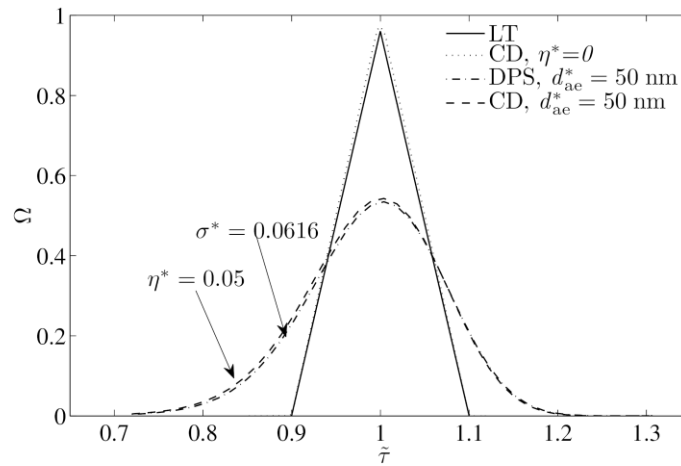


Figure 2. 5 AAC transfer function models with $\delta=0$ and $\beta=0.1$. The models include the non-diffusion limiting trajectory model (solid line), the convective diffusion model when the diffusion term is zero (dotted line), the diffusing particle streamline model (dashed-dot line), and the convective diffusion model (dashed line).

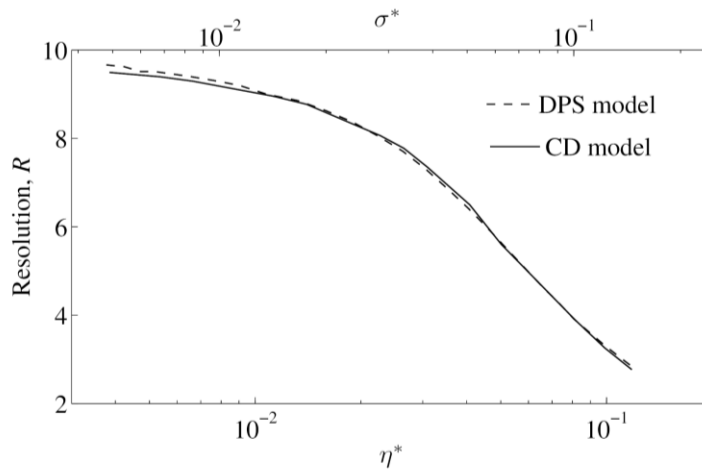
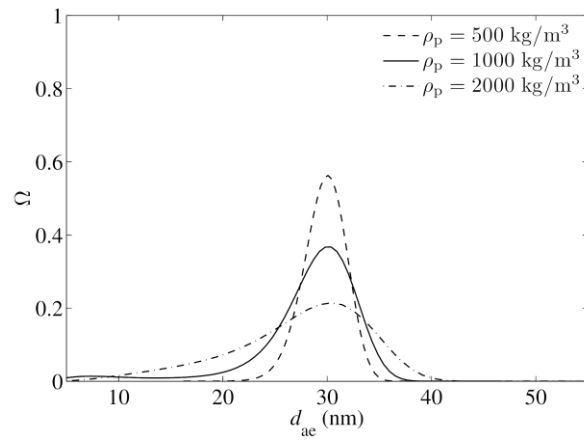


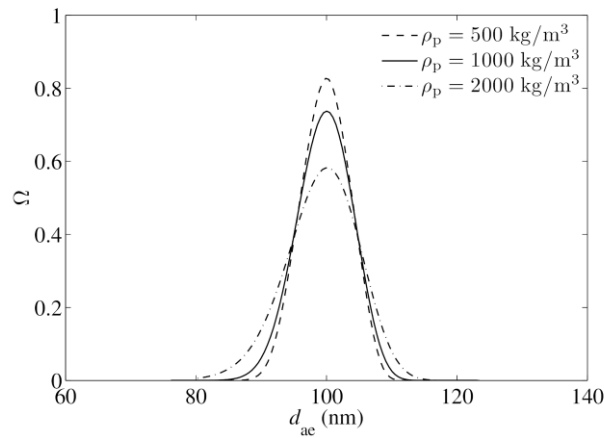
Figure 2. 6 Resolution as a function of η^* and σ^* from the convective diffusion model and diffusing particle streamline model, respectively, for $\delta=0$ and $\beta=0.1$.

Figure 2.7 shows examples of the convective diffusion transfer function for particles with (a) 30 nm, (b) 100 nm, and (c) 300 nm aerodynamic diameters

for the operating conditions shown in Table 2.1. It can be seen that the transfer function with the convective diffusion model is not symmetric. The transfer function on the left side is wider, where the particle size is slightly smaller. The reason for this is that smaller particles have a higher diffusivity than larger particles.



(a)



(b)

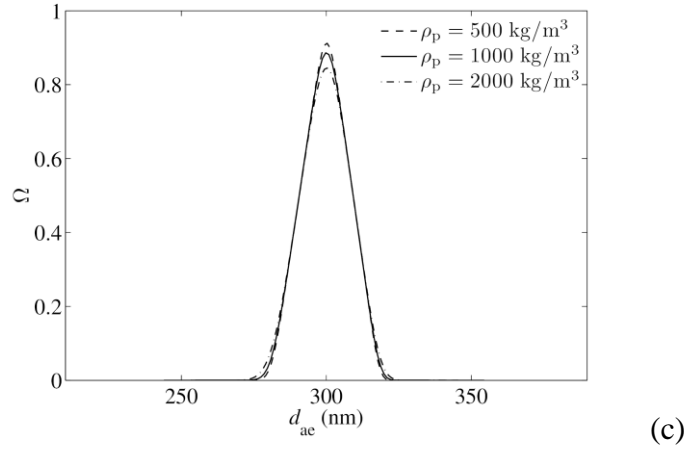


Figure 2. 7 Transfer functions calculated with the convective diffusion model ($\delta=0$ and $\beta=0.1$) of spherical particles with an aerodynamic diameter of (a) 30 nm, (b) 100 nm, (c) 300 nm with particle densities of 500, 1000 and 2000 kg/m^3 for the instrument specifications in Table 2.1.

It should also be noted that the diffusion coefficient (and thus the diffusive transfer function) is a function of the mobility of the particle. The relationship between aerodynamic diameter and mobility diameter for spherical particles can be shown to be,

$$d_{\text{mo}} = d_{\text{ae}} \sqrt{\frac{\rho_0 C_c(d_{\text{ae}})}{\rho_p C_c(d_{\text{mo}})}}, \quad (2.35)$$

where, d_{mo} is the mobility equivalent diameter and ρ_p is the particle density including internal voids (DeCarlo et al., 2004)⁵. As the particle density increases,

⁵ For non-spherical particles the relationship between aerodynamic and mobility diameter is $d_{\text{mo}} = d_{\text{ae}} C_c(d_{\text{mo}}) \sqrt{\frac{\rho_0 C_c(d_{\text{ae}})}{\rho_p C_c^3(d_{\text{ve}})}} \chi^3$ where d_{ve} is volume equivalent diameter including internal void spaces.

for constant aerodynamic diameter, the mobility equivalent diameter decreases, and the diffusion coefficient increases. Therefore, particles with higher particle densities (at a given aerodynamic diameter) will have broader transfer functions and higher diffusional losses as shown in Figure 2.7 for spherical particles where the diffusion coefficient is calculated from the Stokes-Einstein equation ($D=kTB$) using the mobility-equivalent diameter calculated in Equation 2.35. This effect is also seen in particle mass classifiers (CPMA and APM), which classify particles by mass-to-charge ratio yet their diffusive transfer functions are dependent on particle mobility. One application for the AAC would be to measure the aerodynamic-equivalent size distribution of an aerosol by stepping or scanning the rotational speed and measuring the downstream aerosol concentration with a condensation particle counter. However, to invert the AAC measurements using the diffusive transfer function, the mobility of the particle would have to be known or assumed since the diffusive transfer function is dependent on particle mobility.

2.4 Conclusion and summary

The aerodynamic aerosol classifier is an aerosol classifier that classifies particles by their particle relaxation time, from which the aerodynamic equivalent diameter of the particles can be found. Two diffusion models and two non-diffusion models have been used to predict the transfer function of the AAC. An analytical limiting trajectory model and a particle streamline model were used predict the non-diffusion transfer function. A numerical convective diffusion

model and a diffusing particle streamline model were used to model the effects on particle diffusion on the transfer function. The particle streamline models (diffusion and non-diffusion) neglect the divergence of the centrifugal acceleration field in the classifier, but are able to closely approximate the actual classification in the instrument when the gap between the cylinders is small with respect to the radii of the cylinders. In most practical embodiments of the instrument this is expected to be true.

Although the limiting trajectory model and the convective diffusion model are more accurate representations of the classification in the instrument, it is expected that the particle streamline models (diffusion and non-diffusion) will be more widely used for the following reasons: 1) The limiting trajectory non-diffusion particle streamline models are both analytical, but the streamline model has a simpler form and it is simple to see the relationship between the flow rates and the instrument resolution through the parameter β . 2) The convective diffusion model is numerical and modern computers require several minutes to calculate the transfer function. The diffusive streamline model is analytical and the transfer function is quickly calculated. 3) The streamline models for the AAC have very similar form to the streamline models of the differential mobility analyzer, which are widely used and are familiar to many.

Like the DMA it is expected that the AAC will often be used with balanced flows ($Q_a=Q_s$ and $Q_{sh}=Q_{exh}$; $\delta=0$) and with an aerosol to sheath flow ratio of 0.1 ($\beta=0.1$), since this is simple to implement in practice and gives good resolution. Using the proposed dimensions (Table 2.1), the AAC would be able to classify particles over an extremely wide range of 50 nm to 10 μm using rotational speeds ranging from 6800 to 75 rpm and smaller particle sizes could be

classified by using higher rotational speeds. However, the range of an actual instrument will be dependent on its design. The lower size limit will be sensitive to particle diffusion and the maximum rotational speed obtainable and the upper limit will depend on particle impaction in the inlet and outlet of the classifier. Next chapter will demonstrate experimental result from the AAC prototype.

Reference

- DeCarlo, P. F., Slowik, J. G., Worsnop, D. R., Davidovits, P., and Jimenez, J. L. (2004). Particle morphology and density characterization by combined mobility and aerodynamic diameter measurements. Part 1: Theory. *Aerosol Science and Technology*, 38:1185–1205.
- Friedlander, S. (2000). *Smoke, Dust and Haze*. Oxford University Press.
- Gallis, M.A. Torczynski J.R. and Rader, D.J., (2008). Nonzero-concentration boundary condition for advection–diffusion aerosol-transport modeling. *Aerosol Science and Technology*, 42 10, pp. 829–831.
- Hinds, W. C. (1999). *Aerosol Technology: Properties, Behavior, and Measurement of Airborne Particles*. Wiley, New York.
- Hoppel, W.A. (1978). Determination of the aerosol size distribution from the mobility distribution of the charged fraction of aerosols. *Journal of Aerosol Science*, 9 (1), pp. 41-54.
- Knutson, E. O. and Whitby, K. T. (1975). Aerosol classification by electric mobility: Apparatus, theory, and applications, *Journal of Aerosol Science*, vol. 6, pp. 443–451.

-
- Meseguer, A. and Marques, F. (2002). On the competition between centrifugal and shear instability in spiral Poiseuille flow. *Journal of Fluid Mech.* 455, pp. 129–148.
- Olfert, J. and Collings, N.(2005).New method for particle mass classification — The Couette centrifugal particle mass analyzer, *Journal of Aerosol Science*, vol. 36, pp. 1338–1352.
- Stolzenburg, M. R. (1988). An Ultrafine Aerosol Size Distribution Measuring System, PhD Thesis, University of Minnesota.
- Stolzenburg, M. R. and McMurry, P. H. (2008). Equations Governing Single and Tandem DMA Configurations and a New Lognormal Approximation to the Transfer Function, *Aerosol Science and Technology*, 42:6, 421-432.
- Tavakoli, F., Mitra, S. K, Olfert, J. S. (2011). Aerosol penetration in microchannels, *Journal of Aerosol Science*, 42 (5), pp. 321-328.
- Wang, S. C. and Flagan, R. C. (1990). Scanning electrical mobility spectrometer, *Aerosol Science and Technology*, 13:230–240.

Chapter 3

Experimental Validation of the Aerodynamic Aerosol Classifier

In the previous chapter the theoretical models were developed to illustrate the AAC transfer functions. The prototype of aerodynamic aerosol classifier (AAC) was constructed to show the feasibility of the proposed instrument. PSL (polystyrene latex) particles and DOS (DioctylSebacate) were used to calibrate the instrument. A differential mobility analyzer DMA, and a condensation particle counter (CPC) were used to examine the experimental transfer function and to obtain the penetration efficiency of the AAC.

3.1 Introduction

A prototype of the AAC was designed and built. In this chapter, experimental transfer functions from this prototype AAC are examined experimentally and compared with the theoretical models described by Tavakoli and Olfert (2013).

Standard particles with known size and material have often been used to calibrate or validate various aerosol instruments. Polystyrene latex spheres (PSL) have been widely used to validate aerosol classifiers, including the work by Knutson and Whitby (1975) who validated the DMA and Wilson and Liu (1980) who validated the aerodynamic particle sizer (APS). Furthermore, particle mass classifiers like the aerosol particle mass analyzer (APM) and the centrifugal particle mass analyzer (CPMA) have been validated with PSL by Ehara et al. (1996) and Olfert et al. (2006); respectively.

Alternatively, two classifiers can be used in series (tandem) to examine the experimental transfer function and compare it to the theoretical model, as has been done with the DMA (Fissan et al., 1996). Ideally, both classifiers would be identical and operated at the same conditions (Birmili et al., 1997; Martinsson et al., 2001; Li et al., 2006). Also, different classifiers have been used in series to determine the experimental transfer function of a test classifier. These include the evaluation of a three-outlet DMA with a nano-DMA (Giamarelou et al., 2013), and an impactor with a DMA (Fernández de la Mora, et al., 2003).

In this work, the theoretical transfer function of the aerodynamic aerosol classifier is validated using atomized droplets of dioctylesebacate (DOS) and PSL and a DMA.

3.2 Prototype

A schematic of the AAC prototype is shown in Figure 3.1. The aerosol enters the instrument through a hollow shaft, travels through the shaft, and passes through cross-drilled holes in the radial direction. The particles then move radially toward the classification region between the two cylinders. The particles enter the classification region (denoted by the length, L) through a narrow slit on the inner

cylinder. Particle-free sheath flow enters the classification region through a concentric shaft and enters the gap between the cylinders upstream of the aerosol flow. Particles in the classification region are separated by their relaxation time. Particles of a narrow range of relaxation times will exit with the sample flow, while particles with a larger relaxation time impact on the outer cylinder, and particles with a smaller relaxation time will exit with the exhaust flow. The exhaust flow moves radially toward the shaft where it again passes through cross-drilled holes into the center of the shaft and exits the instrument. Before and after the classification region the particles pass through bends and some larger particles may impact onto the walls (which is not accounted for in the theoretical models of the AAC). Also, small particles will be lost because of diffusion effect. Diffusion in the classification region is accounted for in the theoretical model of the AAC but not in the regions before or after. The distance between the aerosol flow entrance and the separation of sample flow (distance L) is 210 mm. The radii of the inner and outer cylinders are 43 mm and 45 mm, respectively.

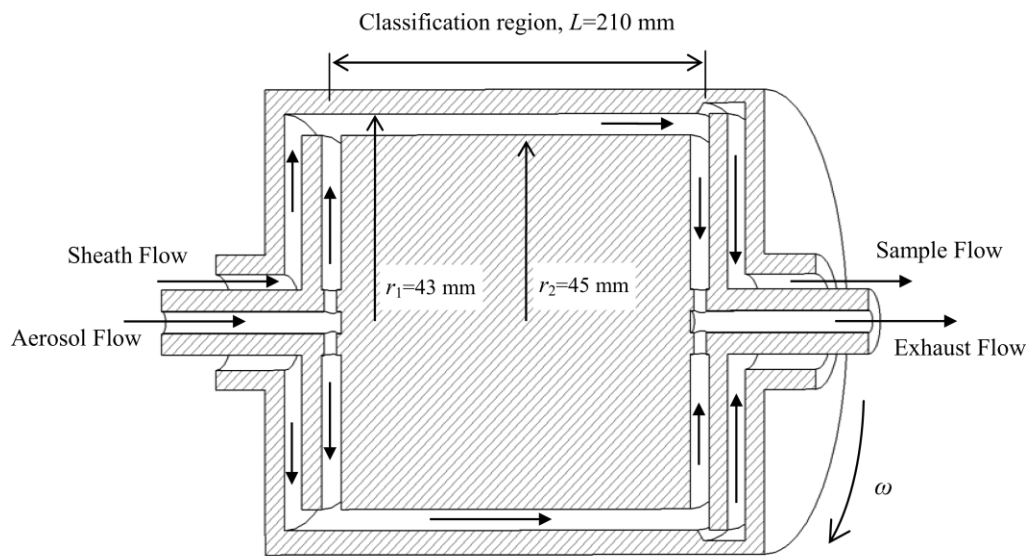


Figure 3. 1 A schematic of the AAC prototype.

Figure 3.2 shows the flow diagram in the AAC. The flows in the AAC can be controlled independently, however it is expected that the AAC will typically be operated in a recirculation mode (as the DMA usually is). In this mode, the aerosol flow and the sample flow are the same and are pulled through the AAC (typically by the CPC pump). Also, the sheath flow is recirculated from the exhaust flow using a blower. Two HEPA capsule (Pall, model 12144) filters have been used before and after the blower to filter the exhaust flow. The flow is controlled using a PID controller by measuring the flow rate with a flow meter (TSI, model 4140) and controlling the speed of the blower. In this work, the AAC was tested at standard conditions for temperature and pressure, and typically with a sheath to aerosol flow ratio of 1:10 with the sheath and exhaust flow rates at 3 L/min and aerosol and sample flow rates of 0.3 L/min.

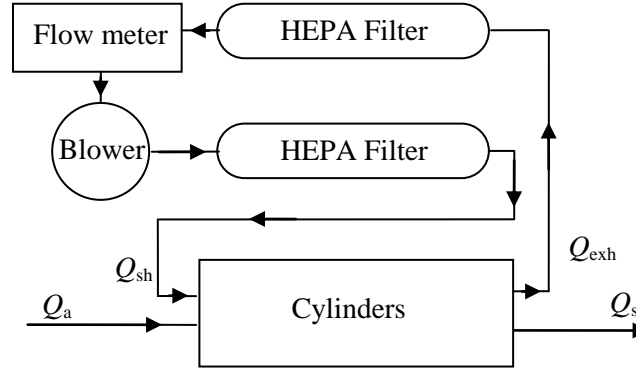


Figure 3. 2 AAC flow diagram.

3.3 Experimental setups for examining transfer function

There are three parameters of interest when comparing the experimental and theoretical transfer functions: i) the value of the particle relaxation time at the maximum of the transfer function (τ^*), ii) shape and width of the transfer

function, and iii) and amplitude of the transfer function (or penetration efficiency of the classifier).

Number of experiments have been conducted to examine the experimental transfer function and to find the efficiency of AAC for different particle sizes. Also, the classifier effective length is determined to correct for the discrepancy between the experimental and theoretical value of τ^* .

For spherical particles the relationship between the aerodynamic diameter and the mobility diameter is,

$$d_{mo} = d_{ae} \sqrt{\frac{\rho_0 C_c(d_{ae})}{\rho_p C_c(d_{mo})}}, \quad (3.1)$$

where d_{mo} is the mobility equivalent diameter and ρ_p is the particle density (including any internal voids in the particle).

The number distribution function $n(d_p)$ is defined as:

$$dN_0 = n(d_p) dd_p, \quad (3.2)$$

where dN_0 is the number of particles in the size interval between d_p and $d_p + dd_p$, where d_p is the particle diameter. d_p can be replaced by d_{ae} (the aerodynamic equivalent diameter) or d_{mo} or $\log d_p$.

The concentration of particles leaving a classifier with the transfer function Ω will be

$$dN = \Omega n(d_p) dd_p, \quad (3.3)$$

When there are two classifiers in series, the concentration will be the result of the convolution of two transfer functions

$$dN = \Omega_1(x)\Omega_2(y)dN_0, \quad (3.4)$$

where x and y can be any properties such as electrical mobility, particle relaxation time, mass, or some equivalent diameter. Multiplying through twice by unity

$$\frac{dN}{dx} = \Omega_1(x)\Omega_2(y) \frac{dN_0}{dy} \frac{dy}{dx}. \quad (3.5)$$

Therefore,

$$N = \int \Omega_1(x)\Omega_2(y) \frac{dN_0}{dy} \frac{dy}{dx} dx. \quad (3.6)$$

In this study, the AAC and DMA are used in series. If the density of the spherical particles is known the AAC transfer function $\Omega_{AAC}(d_{ae}^*, d_{ae}) = \Omega_{AAC}(\tau^*, \tau)$, using Equation (3.1), can be written as $\Omega_{AAC}(d_{mo}^*, d_{mo})$ or $\Omega_{AAC}(Z_p^*, Z_p)$ and therefore the calculation of the convolution of transfer function will be simpler. In this work the non-diffusive particle streamline models of the ACC (Tavakoli and Olfert, 2013) and DMA (Knutson and Whitby, 1975) are used.

In the serial combination of the AAC and DMA, the DMA transfer function $\Omega_{DMA}(Z_p^*, Z_p)$ can also be written as $\Omega_{DMA}(d_{ae}^*, d_{ae})$ if necessary. Therefore the general form will be

$$N = \int n\Omega_1(x)\Omega_2(x)dx. \quad (3.7)$$

3.3.1 Examining transfer function shape using PSL

The schematic of the first experimental setup is shown in Figure 3.3 The types of particles used in this experiment were PSL (Duke Scientific 3000 series)

with particles 104, 154, 302 and 486 nm in diameter. PSL particles were used as a standard because the density (1050 kg/m^3), mean diameter, and the standard derivation of diameter are known. The PSL particles were generated with a Collison atomizer. The PSL particles were generated in a solution of deionized water using TSI aerosol generator (TSI, model 3076). The aerosol flow is dried in a silica-gel diffusion dryer before it enters the AAC. The classified flow is then counted with a condensation particle counter (CPC; TSI, model 3776).

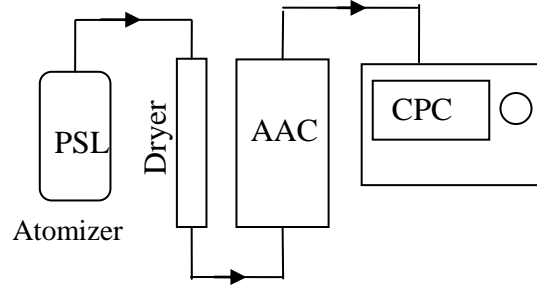


Figure 3. 3 Setup to examine the AAC transfer function using known PSL size (setup I).

PSL aerosols pass through the AAC and are counted with the CPC. The rotational speed of the AAC, ω , was stepped to measure the particle concentration counted by the CPC as a function of the rotational speed. Numerically, the convolution shown in Eq. 3.7 can be used using the PSL size distribution and the AAC transfer function.

$$N(\omega_i) = \int \eta_{AAC} n_{PSL}(d_{ae}) \Omega_{AAC}(d_{ae,i}^*, d_{ae}) dd_{ae} \quad (3.8)$$

where N is the particle concentration measured with the CPC, η_{AAC} is the AAC penetration efficiency, Ω_{AAC} is the AAC transfer function, and n_{PSL} is the PSL particle size distribution which can be assumed to be a normal distribution.

$$n_{PSL} = \frac{1}{\sigma_{PSL}\sqrt{2\pi}} e^{-\frac{(d_{PSL}-d_p)^2}{2\sigma_{PSL}^2}} \quad (3.9)$$

where σ_{PSL} is the standard deviation of PSL particle concentration and d_{PSL} is the mean. η_{AAC} is considered to be constant over the PSL size distribution.

3.3.2 Examining transfer function shape using DOS

Figure 3.4 shows the experimental setup (setup II) to compare the theoretical and experimental AAC transfer functions using a DMA. DOS (DioctylSebacate) or bis (2-ethylhexyl) sebacate particles are atomized using the same atomizer. The AAC is set to a constant rotational speed, ω , ($d_{ae}^* = \text{constant}$) and the DMA (TSI, model 3081) and CPC (same as above) are used after the AAC. The DMA was used with balanced flows with sheath and exhaust flows of 3 L/min, and sample and aerosol flows of 0.3 L/min.

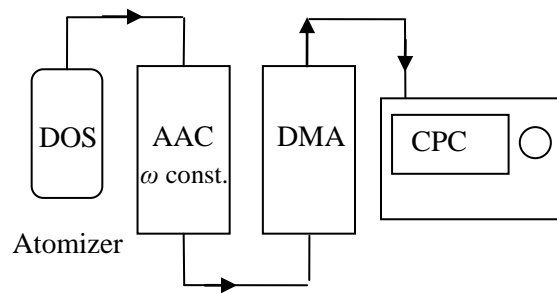


Figure 3. 4 Setup to examine the experimental transfer function with DOS (Setup II).

The DMA voltage is stepped through a range of voltages and the particle concentration is measured for each voltage step. The DMA mobility diameter is

converted to the aerodynamic-equivalent diameter assuming that the DOS particles are spherical with a density of 913 kg/m^3 .

It should be noted that the multiple charged particles are far from each other in the aerodynamic space and also the AAC transfer function is narrow. The DMA voltage was only stepped to measure the singly-charged particles.

$$\begin{aligned}
 N(V_i) & \\
 &= \int \eta_{\text{DMA}} \eta_{\text{AAC}} \Omega_{\text{AAC}}(d_{\text{mo}}^*, d_{\text{mo}}) \Omega_{\text{DMA}}(d_{\text{mo},i}^*, d_{\text{mo}}) n_{\text{DOS}}(d_{\text{mo}}) dd_{\text{mo}} \quad (3.10)
 \end{aligned}$$

where $\Omega_{\text{AAC}}(d_{\text{mo}}^*, d_{\text{mo}})$ is obtained from $\Omega_{\text{AAC}}(d_{\text{ae}}^*, d_{\text{ae}})$ using Equation 3.1, V is the DMA voltage, and η_{DMA} and η_{AAC} are considered constant for each rotational speed.

3.3.3 AAC efficiency using PSL

The theoretical transfer function derived by Tavakoli and Olfert (2013) gives the probability of a particle can pass through the classification region as a function of the particle's relaxation time (or aerodynamic diameter). However, a fraction of these particles cannot pass through the classifier due to impaction and diffusion inside of the instrument, as the particles move into and out of the classification region. The penetration efficiency, η_{AAC} , is the ratio of the number of particles that pass through the instrument to the number of particle that could have passed in the absence of diffusion and impaction.

Figure 3.5 (experimental setup III) provides the schematic of the experimental setup to obtain the penetration efficiency of particles that the AAC classifies. The PSL particles contain surfactant to stabilize the particles in water and to keep them from agglomerating. Nebulized PSL also contains surfactant

with a much smaller size distribution than the PSL particles. To omit the effect of the surfactant, the DMA was used after the dryer to select only a portion of PSL particles, where the DMA was set to the mean size of the PSL distribution. The particle concentration is measured after the DMA (before entering the AAC) using the CPC. The AAC rotational speed is stepped and the particle concentration is recorded after the AAC for different rotational speeds. The convolution of the DMA transfer function and AAC transfer function on PSL particles gives the particle concentration at the AAC output. The ratio of the experimental concentration to the theoretical non-diffusion model gives the AAC efficiency.

$$N_{\text{out}}(\omega_i) = \int \eta_{\text{AAC}} \eta_{\text{DMA}} \Omega_{\text{DMA}}(d_{\text{ae}}^*, d_{\text{ae}}) \Omega_{\text{AAC}}(d_{\text{ae},i}^*, d_{\text{ae}}) n_{\text{PSL}}(d_{\text{ae}}) dd_{\text{ae}}. \quad (3.11)$$

where $\Omega_{\text{DMA}}(d_{\text{ae}}^*, d_{\text{ae}})$ is obtained from $\Omega_{\text{DMA}}(d_{\text{mo}}^*, d_{\text{mo}})$ using Equation 3.1. The CPC counts the particle concentration before it enters the AAC as

$$dN_{\text{in}} = \eta_{\text{DMA}} n_{\text{PSL}}(d_{\text{mo}}) \Omega_{\text{DMA}}(d_{\text{mo}}^*, d_{\text{mo}}) dd_{\text{mo}}. \quad (3.12)$$

From the theory $\Omega_{\text{AAC}}(d_{\text{ae},i}^*, d_{\text{ae}})$ is known and η_{AAC} can be calculated by Equation 3.12.

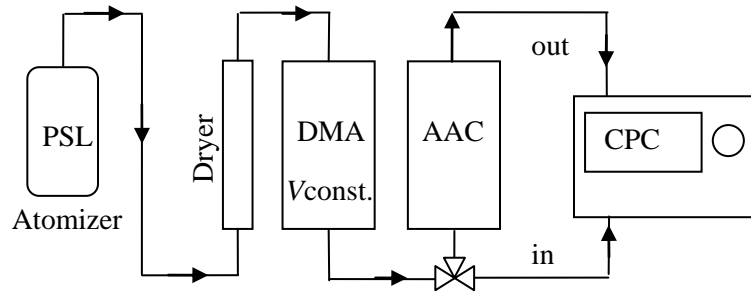


Figure 3. 5 Setup to obtain the AAC efficiency (Setup III).

3.3.4 AAC efficiency using DOS

The penetration efficiency of this prototype AAC was also measured using a DOS aerosol with a scanning mobility particle sizer (SMPS) and an AAC-CPC system in tandem as shown Figure 3.6 (experimental setup IV). DOS particles are generated using the aerosol generator (TSI model number 3076). The SMPS is used to measure the mobility particle distribution which is converted to the aerosol dynamic particle size distribution. From the particle distribution and the AAC transfer function, the number of particle that is supposed to pass through the AAC can be calculated theoretically. This method is likely not as accurate as the PSL method described above due to the uncertainties in the SMPS data inversion process, but it can be used to measure the wide range of particle sizes.

The ratio of the actual to theoretical particle concentration is considered as the penetration efficiency.

$$N(\omega_i) = \int \eta_{AAC} n_{DOS}(d_{ae}) \Omega_{AAC}(d_{ae}^*, d_{ae}) dd_{ae} \quad (3.13)$$

The SMPS gives the value of $n_{DOS}(\log(d_{mo})) = dN/d\log(d_{mo})$ using Equation 3.1. The DOS size distribution will be a function of the aerodynamic diameter $n_{DOS}(d_{ae})$, and η_{AAC} can be calculated from Equation 3.13.

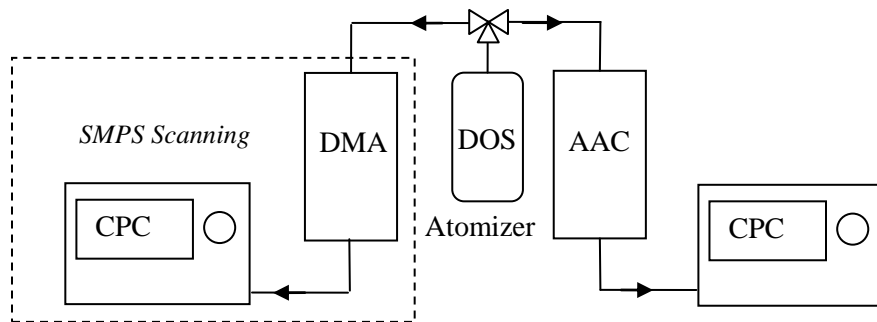


Figure 3. 6 Experimental setup (IV).

3.4 Experimental results and discussion

3.4.1 AAC Effective length

From experimental set up I (Figure 3.3) and from experimental set up II (Figure 3.4), aerodynamic diameter of PSL and DOS particles can be determined. In setup I there are four sizes of 104, 154, 302 and 486 nm for PSL. In setup II, a narrow range of DOS droplets will be selected from a larger distribution of droplets generated in the atomizer. The peak particle size that measured with AAC can be compared with the expected value. A comparison of the AAC-measured relaxation time (τ^*) and the expected relaxation time of the PSL and DOS particles is shown in Figure 3.7. The relaxation time measured by the AAC is slightly lower than the expected relaxation time of the PSL or DMA-classified DOS particles, although within the expected uncertainty. The data are quite linear, in terms of particle relaxation time. Therefore, we can use an effective length to correct for the systematic bias. Figure 3.7 shows a plot of the data, which have been fit with a line using least-squares linear regression. The effective length will be the actual length of the classifier ($L=210$ mm) divided by the slope of the fit line. Therefore, the effective length will be: $L_{\text{eff}} = L / 1.0293 = 204.0$ mm. The effective length will be used in the calculations of the instrument corrected transfer function. The uncertainty in the effective length is ± 5 mm, which gives the uncertainty in aerodynamic size of 2.5%.

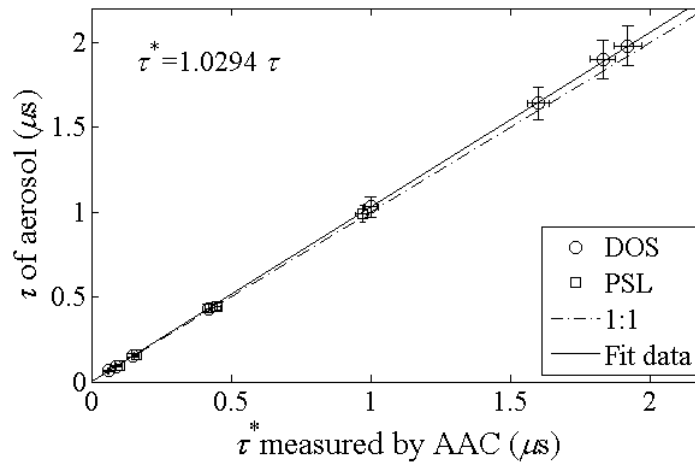
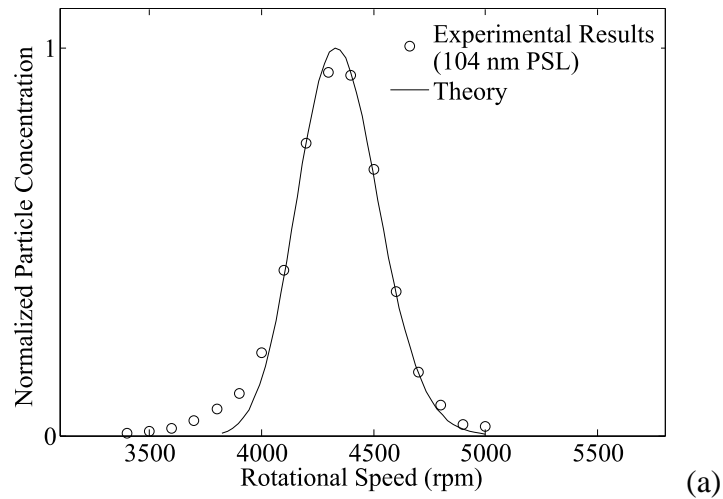


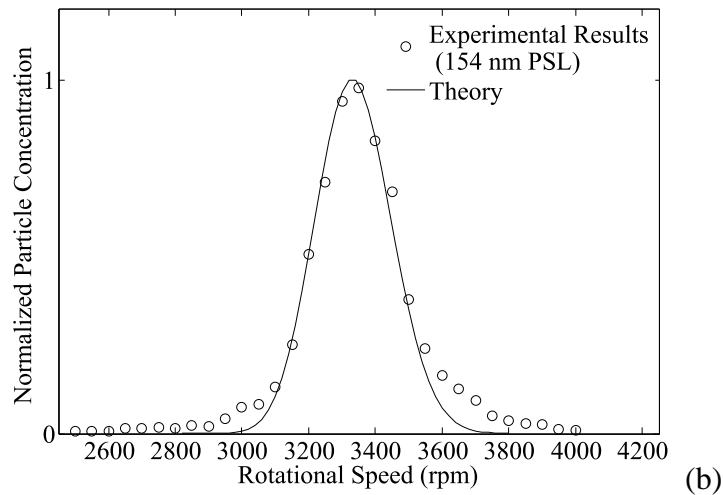
Figure 3. 7 Calibration curve for the AAC, where τ is the particle relaxation time of PSL and DOS particles and τ^* is the expected instrument response from the theory. The error bars represent a 95% confidence interval in the uncertainty of the DMA (estimated to be 3%, Kinney *et al.*, 1991) and PSL spheres (~2–3% depending on size) and 3% in uncertainty in density of DOS.

3.4.2 Experimental transfer function

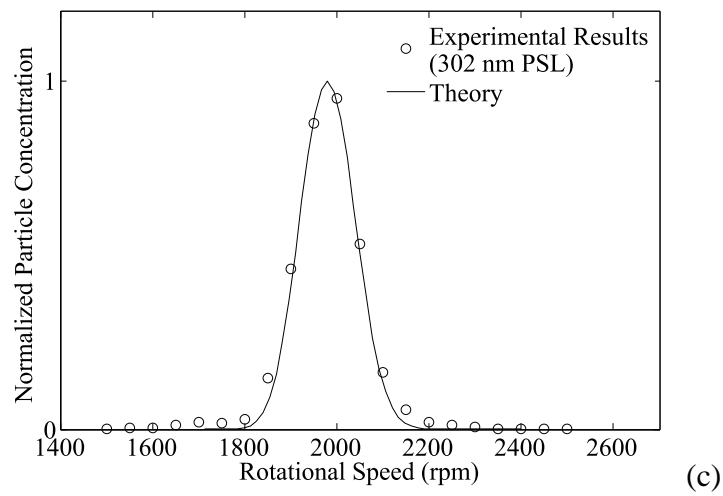
In setup I, PSL particles of a given size are atomized and the particle concentration after the AAC is measured with a CPC, when the AAC is stepped through different rotational speeds. Figure 3.8 shows the normalized particle concentration from setup I (Figure 3.3) and the mathematical model representing the convolution of the AAC transfer function and the PSL size distribution. The model is adjusted with the proper effective length so that peak matches the experimental peak, therefore only the shape and the width of the transfer function can be compared.



(a)



(b)



(c)

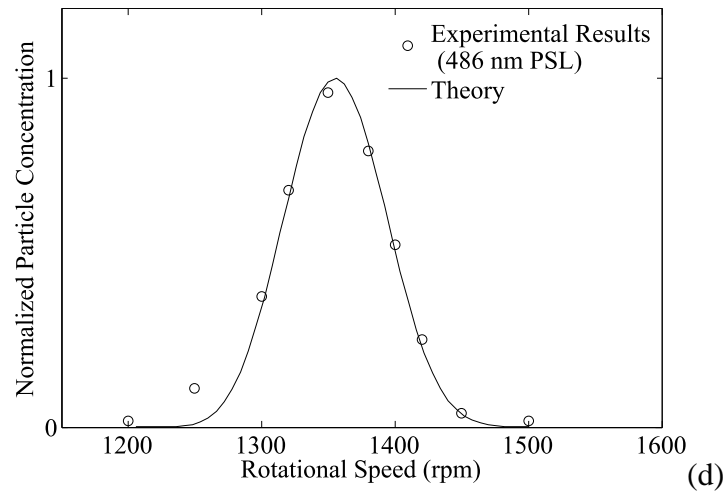
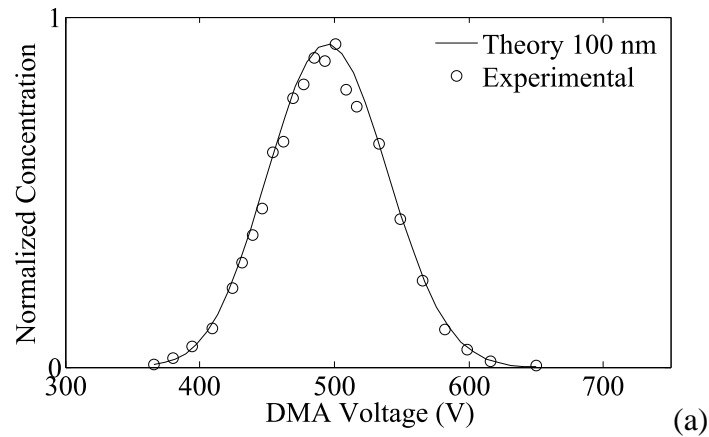


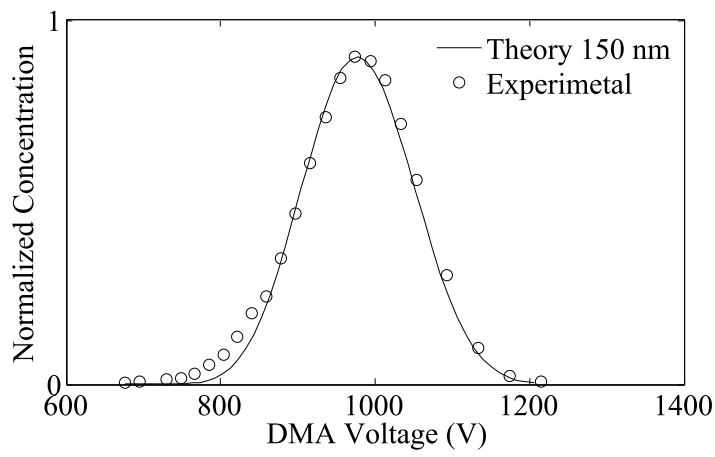
Figure 3. 8 Normalized PSL particle concentration versus AAC rotational speed (setup I).

In setup II (Figure 3.4), AAC separates a narrow range of particle sizes from the DOS droplet distribution and then the combination of a DMA and CPC is used to measure the particle concentration in this range. Figure 3.9 shows the normalized DOS particle concentration coming out of the AAC and DMA at a constant rotational speed for AAC and DMA voltage stepped. Mathematical model of this experiment is representing in Equation 3.10.

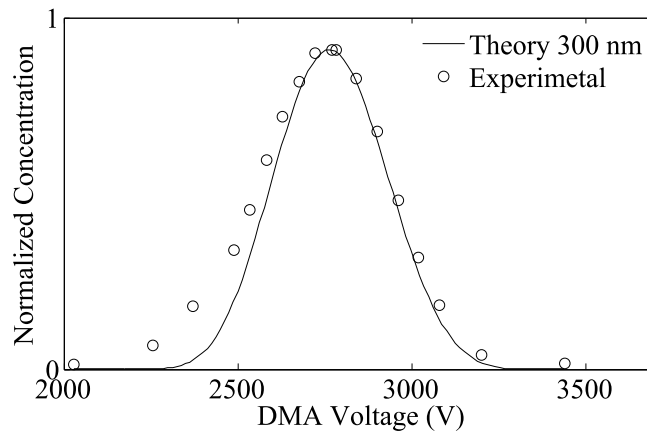
In general, the PSL and DOS experimental results agree well with the theoretical response spectrum. The experimental results agree especially well near the peak of the distribution. Most of the data shows that the experimental spectrum is wider than the theoretical spectrum near the ends of the distribution. This could be caused by differences in the experimental and theoretical transfer functions of either the AAC or DMA.



(a)



(b)



(c)

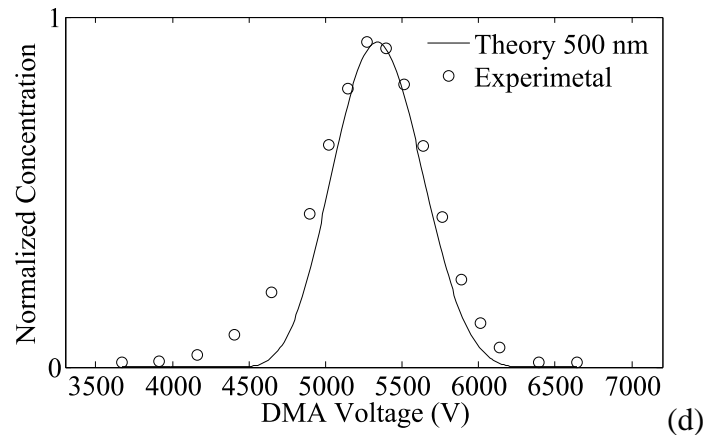


Figure 3. 9 Experimental and theoretical DOS concentration (setup II).

3.4.3 Resolution

Setup II (Figure 3.4) has been used to examine the resolution of the transfer function by using different sheath to aerosol flow ratios. Figure 3.10 shows the effect of sheath flow on the resolution of the AAC transfer function. AAC was operating with balanced flows with the aerosol and sample flows at 0.3 L/min. The ratio of the sheath flow to aerosol flow changes the transfer function width as shown by Tavakoli and Olfert (2013). To classify the same aerodynamic particle size (300 nm), for a different sheath flow, the AAC rotational speed was also changed. As expected, the transfer function width increases by decreasing the sheath flow. It can be seen in Figure 3.10 that the theoretical prediction has a narrower system response curve and, the difference between the theory and the experiments is more noticeable for small ratio of aerosol flow to sheath flow. The experimental resolution of the AAC is 17%, 35% and 50% higher than its theoretical value for sheath flow of 3 L/min, 1 L/min and 0.75 L/min respectively. Since the DMA was operated at the same condition in all these experiments, the increased broadening is due to widening in the AAC transfer function.

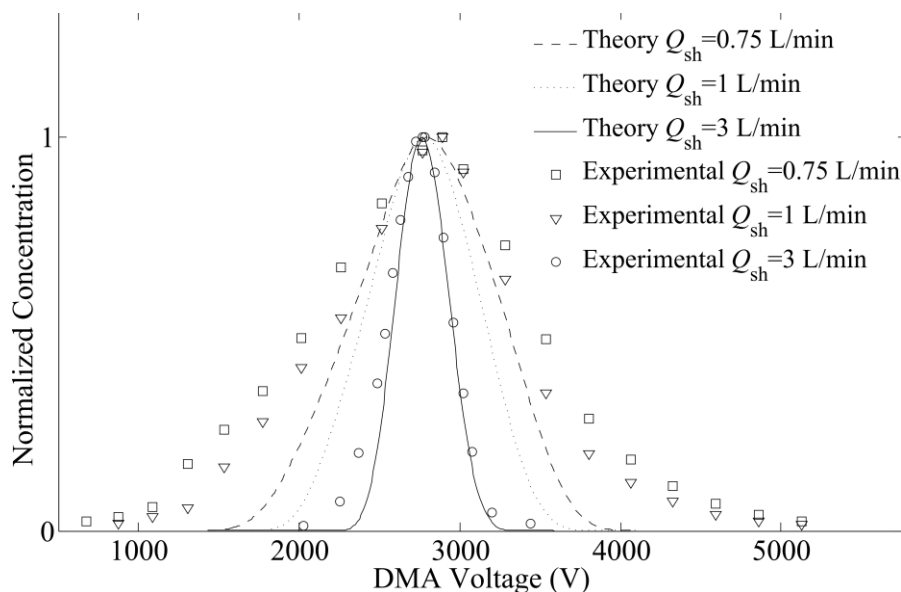


Figure 3. 10 AAC resolution using DOS with sample flow of 0.3 L/min and different sheath flow (setup II).

3.4.4 AAC Efficiency

Figure 3.11 shows the efficiency of the AAC for the particle range of 95 to 910 nm. Two different setups were used for calculating the AAC efficiency. In setup III (Figure 3.5) PSL particles pass through the AAC. A DMA is used to select the PSL particles (and remove the surfactant particles) before the AAC. The particle concentration pre- and post-AAC is counted with the CPC, then the AAC efficiency is calculated using Equations 3.11 and 3.12. Figure 3.10 shows efficiency of 20% to 40% for the range between 104 and 486 nm for PSL particles.

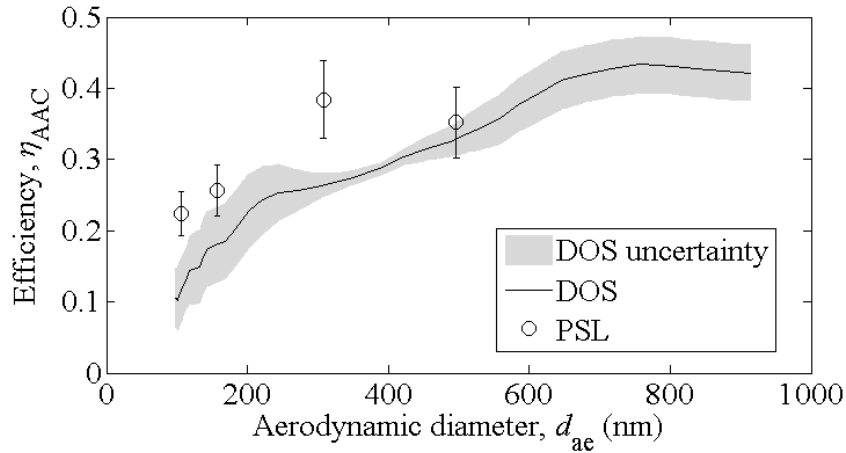


Figure 3. 11 AAC efficiency using DOS and PSL particles (setup III and IV).

In setup IV (Figure 3.6), the DOS size distribution, n_{DOS} , is obtained by SMPS scanning. Then, the AAC is stepped through different rotational speeds and the DOS particles passing through the AAC are counted with a CPC. Using the non-diffusion AAC transfer function in Equation 3.13 gives the theoretical value for the particle concentration. Comparing experimental and theoretical gives the AAC efficiency, η_{AAC} . Figure 3.10 shows efficiency of 10% and 42% for particles from 95 nm to 910 nm. The shaded region is the standard deviation from the experimental measurements, and does not include multiple charging correction for SMPS.

Both experiments show the efficiency of the AAC is lower for smaller particle size because of diffusion effect and the fact that the instrument rotates at higher speed increases the impaction in the inlet and outlet of the instrument. The uncertainty in measuring the size distribution of DOS using SMPS is high which increases the uncertainty in efficiency calculations.

Although, the efficiency seems low it is comparable, or better than the efficiency of the DMA. In the DMA the particles are neutralized to create an equilibrium charge distribution, which results in many particles are negatively-charged or neutral. The charging efficiency of a neutralizer ranges from 21% – 11% for singly charged particles over the size range of 95 to 910 nm, respectively. Therefore, the AAC is better suited than a DMA in applications where higher particle concentrations are required.

3.5 Summary

The AAC classifies particles by their aerodynamic size. One AAC prototype was built to be tested, and compared with the theoretical models developed earlier (Tavakoli and Olfert, 2013). The AAC prototype was tested over a range of particle sizes. It was found that the transfer function of the AAC agreed well with the theoretical model. The aerodynamic diameter classified by the AAC is slightly larger than the expected aerodynamic diameter calculated and measured by the DMA. This can be compensated for by modifying the effective length of the instrument. The calibration is conducted using data from experiments with PSL particles and DOS droplets.

It was also found efficiency of AAC is higher for larger particles and the efficiency changes from 10% to 42% for particles from 95 nm to 910 nm size. Future work will be focused on re-designing the inlet and outlet of the classifier to increase its efficiency.

Reference

- Baron P. A. and Willeke K., (2001), *Aerosol Measurement - Principles, Techniques, and Applications* -2nd Edition, John Wiley & Sons, ISBN 0-471-35636-0
- Birmili W., Stratmann F., Wiedensohler A., Covert D., Russell L. M. and Berg O., (1997). Determination of Differential Mobility Analyzer Transfer Functions Using Identical Instruments in Seriespages, *Aerosol Science and Technology*, 27(2), 215-223.
- Ehara, K., Hagwood, C., and Coakley, K. J. (1996). Novel method to classify aerosol particles according to their mass-to-charge ratio – aerosol particle mass analyser. *Journal of Aerosol Science*, 27(2):217–234.
- Fernández de la Moraa, J., de Juana, L., Liedtkeb, K., Schmidt-Ottc, A., (2003).Mass and size determination of nanometer particles by means of mobility analysis and focused impaction. *Journal of Aerosol Science* Volume 34, Issue 1, Pages 79–98.
- Fissan H., Hummes D., Stratmann F., Büscher P., Neumann S., Pui D. Y. H., Chen D. (1996), Experimental Comparison of Four Differential Mobility Analyzers for Nanometer Aerosol Measurements, *Aerosol Science and Technology*, 24 (1), 1-13.
- Giamarelou M., Stolzenburg M., Chen D., and Biskos G., (2013),Comparison Between the Theoretical and Experimental Performance of a Differential Mobility Analyzer with Three Monodisperse-Particle Outlets, *Aerosol Science and Technology*,47(4), 406-416.
- Kinney, P. D., Pui, D. Y. H., Mulholland, G. W. and Bryner, N. P. (1991). Use of the Electrical Classification Method to Size 0.1 μm SRM Particles—A Feasibility Study. *J. Res. Natl. Inst. Stand. Technol.*, 96: 147–176.

-
- Knutson, E. O., and Whitby, K. T. (1975). Aerosol classification by electric mobility: Apparatus, theory, and applications. *Journal of Aerosol Science*, 6:443–451.
- Li W., Li L. and Chen D., (2006). Technical Note: A New Deconvolution Scheme for the Retrieval of True DMA Transfer Function from Tandem DMA Data, *Aerosol Science and Technology*, 40(12),1052-1057.
- Martinsson B. G., Karlsson M. N. A. and Frank G. (2001),Methodology to Estimate the Transfer Function of Individual Differential Mobility Analyzers, *Aerosol Science and Technology*, 35(4), 815-823.
- Olfert, J.S., Reavell, K. StJ., Rushton, M.G., Collings, N. (2006). The experimental transfer function of the Couette centrifugal particle mass analyzer *Journal of Aerosol Science*, 37 (12), pp. 1840-1852
- Tavakoli, F., and Olfert, J. S. (2013). An Instrument for the Classification of Aerosols by Particle Relaxation, Time: Theoretical Models of the Aerodynamic Aerosol Classifier, *Aerosol Science and Technology*, 47:8, 916-926.
- Wilson, J.C., Liu, B.Y.H. (1980). Aerodynamic particle size measurement by laser-doppler velocimetry, *Journal of Aerosol Science*, 11 (2), pp. 139-150.

Chapter 4

Determination of particle mass, effective density, mass-mobility exponent and dynamic shape factor using an aerodynamic aerosol classifier and a differential mobility analyzer in tandem

In this chapter, a differential mobility analyzer (DMA) and an aerosol aerodynamic classifier (AAC) are used in tandem to measure the effective density, shape factor and the mass of soot and dioctylsebacate (DOS) particles.

4.1 Introduction

Multiple aerosol instruments are often used in tandem, or in series, to determine particle properties that cannot be obtained by one instrument alone. In the majority of these applications the first instrument in the series is the differential mobility analyzer (DMA), which classifies particles by electrical mobility. The particles exiting the DMA, which are monodisperse in terms of electrical mobility (but not necessarily mobility), are then measured by another instrument or classifier. An extensive review of these systems is given by Park et al (2008). For example, effective density, mass-mobility exponent, aerodynamic

diameter, and dynamic shape factors have been measured with tandem systems of a DMA and a mass classifier (aerosol particle mass analyzer (APM) or centrifugal particle mass analyzer (CPMA); eg. McMurry et al., (2002), Olfert et al. (2007)), or DMA and impactor (e.g. Kelly and McMurry (1992), Ahlvik et al. (1998), Maricq et al. (2000), and Maricq and Xu (2004)), or DMA and mass spectrometer (Larriba et al., 2011), or DMA and aerosol mass spectrometer (using the vacuum aerodynamic diameter measurement on the inlet of the aerosol mass spectrometer; e.g. De Carlo et al. (2004)). In some experiments two DMAs are used in tandem where the aerosol classified by the first DMA is conditioned and the change in the size of the particles is measured by the second DMA. These tandem DMA systems are used to measure: hygroscopicity by conditioning the sample through humidification (hygroscopicity tandem differential mobility analyzer; eg. Liu et al. (1978); Rader and McMurry (1986)), or volatility by conditioning with an evaporator (volatility tandem differential mobility analyzer; eg. Rader et al. (1987)).

In this work we present a tandem measurement system using an aerodynamic aerosol classifier (AAC) and a differential mobility analyzer. The AAC consists of two concentric cylinders (or classification column) that rotate at the same rotational speed. Polydisperse aerosol enters the space between the cylinders and is carried with particle-free sheath flow through the classification column. The particles in the classification column experience a centrifugal force that causes them to move toward the outer cylinder. At the end of the classification column, there is a small slit on the outer cylinder where particles with a narrow range of particle relaxation time exit the classifier with the sample flow. The operation of the AAC and models of its transfer function is described in detail by Tavakoli and Olfert (2013).

The AAC produces a monodisperse aerosol classified by particle relaxation time (from which the aerodynamic equivalent diameter of the particle can be calculated). The classification of particles in the AAC is not dependent on the particle electric charge, so the aerosol classified by the AAC is truly monodisperse (particles of a narrow range of aerodynamic diameter), unlike the DMA which produce an aerosol with multiple sizes depending on the electrical charge.

Here we demonstrate the use of a tandem AAC-DMA system to measure, or estimate, particle mass, volume, dynamic shape factor, and effective density. The test particles used are soot generated from a diffusion flame, which are non-spherical particles formed through the aggregation of individual spherules and are often recognized as fractal-like, and atomized droplets of dioctylsebacate (DOS), which are spherical and have a known material density.

4.2 Experimental setup

Figure 4.1 shows the schematic diagram of the experimental setup. The experiment consists of an aerosol source (soot or DOS), an aerodynamic aerosol classifier (AAC), a DMA (TSI, Inc., Model 3080), and a condensation particle counter (CPC; TSI, Inc., Model 3776).

The inverted burner that is used to produce soot particles is similar to the design of Stipe et al. (2005) and Ghazi et al. (2013). Stipe et al. (2005) introduced an inverted co-flow diffusion flame, which is capable of generating stable soot in a wide range of sizes and concentrations. The buoyant gases from the downward combustion flow prevent the flame from flickering. Therefore, the concentration and size distribution of generated soot are steady with respect to time. The inverted burner used in this study consists of a quartz tube of 48 cm length and

48 mm diameter. Methane is supplied to the burner via a mass flow controller (Cole-Parmer, Vernon Hills, IL, USA, Model 32907-69) at flow rates of 1.26 SLPM. Combustion air is supplied at 18SLPM flow rate (Omega, Inc., Dewitt, NY, USA, Model FMA-774-V) to reach a global equivalence ratio of 0.67. Another mass flow controller (Omega, Inc., Dewitt, NY, USA, Model FMA-774-V) is used to inject dilution air into the exhaust at a flow rate of 29 SLPM to maintain a dilution ratio of 3.5. Soot particles are sampled 50 cm after the dilution point.

The dioctylsebacate aerosol is generated through atomization using a aerosol generator (TSI, Model 3076). DOS is a liquid (density of 913 kg/m^3) at room temperature and it has low vapour pressure. Since the DOS particles are liquid at room temperature it is assumed that they are spherical. Also, the vapour pressure of DOS is small so it is assumed that the DOS does not evaporate and change the particle size as it is classified by the AAC and DMA.

Aerosol sample is passed through the AAC-DMA in serial (tandem). The AAC is set to a constant rotational speed to separate particles by relaxation time (or aerodynamic size). The voltage of the DMA is then stepped and the particle concentration is measured with the CPC. The concentration of particles at the exit of the DMA will be the convolution of the transfer functions of the two classifiers;

$$N = \int \Omega_{\text{DMA}}(Z_p) \Omega_{\text{AAC}}(\tau) \frac{dN_0}{d\tau} \frac{d\tau}{dZ_p} dZ_p \quad (4.1)$$

where τ is the particle relaxation time, Z_p is the particle electrical mobility, N is the particle concentration measured with the CPC, Ω_{AAC} is the AAC transfer function, Ω_{DMA} is the DMA transfer function, and

$$dN_0 = n_0(\tau)d\tau \quad (4.2)$$

where n_0 is the particle size distribution entering the AAC. Figure 4.2 shows an example of the particle concentration exiting the DMA as a function of DMA voltage when the AAC is set to 3000 rpm and soot particles are passing through the tandem AAC-DMA. Monodisperse particles that exit AAC will obtain single or multiple elementary electric charges in the radioactive source (Kr-85) in the DMA. Figure 4.2 shows two peaks – multiply-charged particles have a higher electrical mobility therefore, the peak on the right represents the single charged particles, and the peak on the left represents the multiply-charged particles.

The soot particles measured in this study range in size of 95 to 637 nm in terms of mobility equivalent diameter, which corresponds to 84 to 232 nm in aerodynamic equivalent diameter. The size of DOS particles are in range of 88 to 750 nm in terms of mobility equivalent diameter.

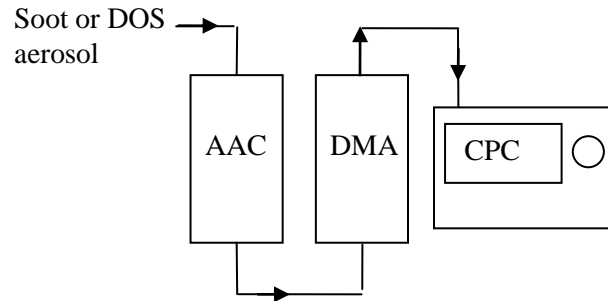


Figure 4. 1 Schematic diagram of the experimental setup.

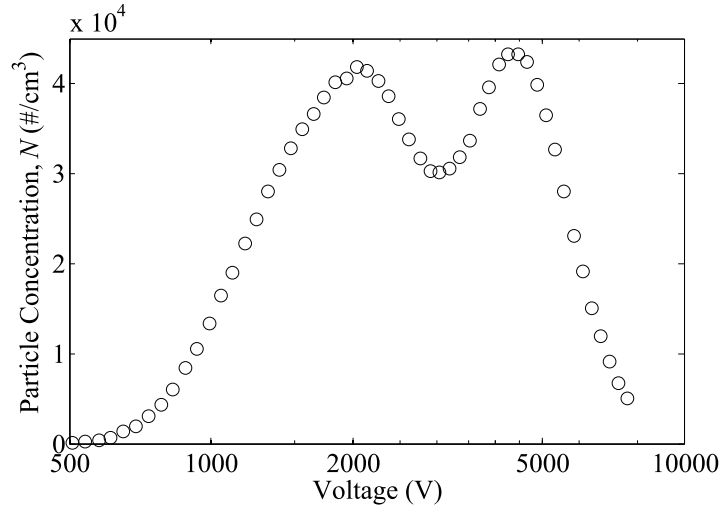


Figure 4. 2 Soot particle concentration at the exit of the AAC-DMA.

4.3 Results and discussion

4.3.1 Particle Mass

The particle relaxation time, τ , is defined as the particle's mobility, B multiplied by mass m ,

$$\tau = Bm, \quad (4.3)$$

where mobility can be expressed as

$$B = \frac{C_c(d_{mo})}{3\pi\mu d_{mo}}, \quad (4.4)$$

where d_{mo} is the mobility diameter; μ is the viscosity of the carrier gas, and C_c is the Cunningham slip correction factor. Also, it can be shown that the aerodynamic diameter is a function of the particle relaxation time regardless of density and shape of particle (see Appendix A):

$$\tau = \frac{C_c(d_{ae})\rho_0 d_{ae}^2}{18\mu} \quad (4.5)$$

where μ is the viscosity of the carrier gas and d_{ae} is the aerodynamic diameter of the particle. The particle relaxation time and mobility are measured from the AAC and DMA, respectively. Therefore, Equation 4.3 can be solved for m , when both the relaxation time and mobility are known.

McMurry et al. (2002) used a tandem DMA–APM setup to measure mass-mobility relationship and the same technique has been implemented for a DMA-CPMA system (Olfert et al., 2007; Ghazi et al., 2013). It has been shown that the relation between mass and mobility diameter often follows a power-law relationship (Park et al., 2003)

$$m = C d_{m0}^{D_{fm}}, \quad (4.6)$$

where C is a constant and D_{fm} is the mass-mobility exponent. Figure 4.3a shows the particle mass of soot generated by the inverted burner for a range of mobility diameters, using the tandem AAC-DMA system. A power function is fit to the experimental results to calculate the mass–mobility exponent. The mass-mobility exponent for this soot was found to be 2.17, which is typical of soot particles (~2.2; Sorensen 2011). The mass mobility relationship of DOS particles is shown in Figure 4.3b. As expected the mass–mobility exponent is approximately 3 as the DOS particles are spherical.

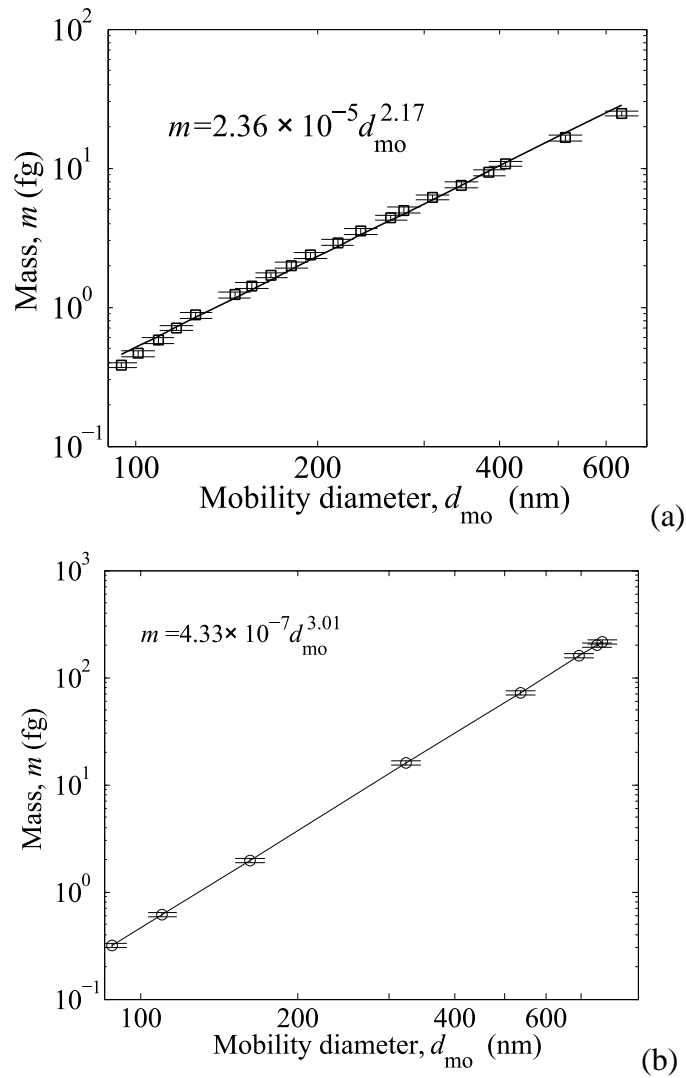


Figure 4. 3 The particle mass-mobility relationship for (a) soot particles and (b) DOS particles.

4.3.2 Effective density

The particle effective density is an important parameter because it can be used to convert size distributions to mass distributions (Friedlander, 2000). Various definitions of effective density are provided in the literature, and a review of these definitions are given by DeCarlo et al., 2004. All the definitions are intended to demonstrate the irregularity in the shape of a particle.

A common definition of effective density, ρ_{eff} , is particle mass divided by the volume of a spherical particle with a diameter equal to the mobility diameter,

$$\rho_{\text{eff}} = \frac{m}{\frac{\pi}{6}d_{\text{mo}}^3} = \frac{6C}{\pi}d_{\text{mo}}^{(D_{\text{fm}}-3)}. \quad (4.7)$$

For spherical particles the effective density equals the particle density including internal voids. For spherical particles without internal voids, the effective density is equal to the material density of the particle. In non-spherical particles, the effective density is lower than the material particle density and for fractal-like agglomerates like soot, the effective density will decrease for larger particle sizes. Effective density demonstrates the effect of the external pseudo-void fraction because of the external physical morphology and not the internal void fraction.

Figure 4.4 shows the effective density of soot and DOS particles as a function of mobility diameter. The effective density of DOS particles is constant with respect to mobility diameter at $903 \pm 89.6 \text{ kg/m}^3$, which is almost equal to the material density of DOS, $913 \pm 3 \text{ kg/m}^3$. As expected, the effective density of the soot particles decreases as a function of mobility diameter. From this figure it is apparent that the effective density function deviates from the power-law relationship at small particle sizes. The reason for this is unclear; however, Ghazi et al. (2013) found that the inverted burner tested here produced particles with two different morphologies: i) aggregates with well defined primary particles and open structures typical of combustion generated soot, and ii) aggregates with much smaller primary particle size and compact structures. The deviation from the power-law relationship at smaller sizes may be due to a transition between the relative concentrations of these two particle types.

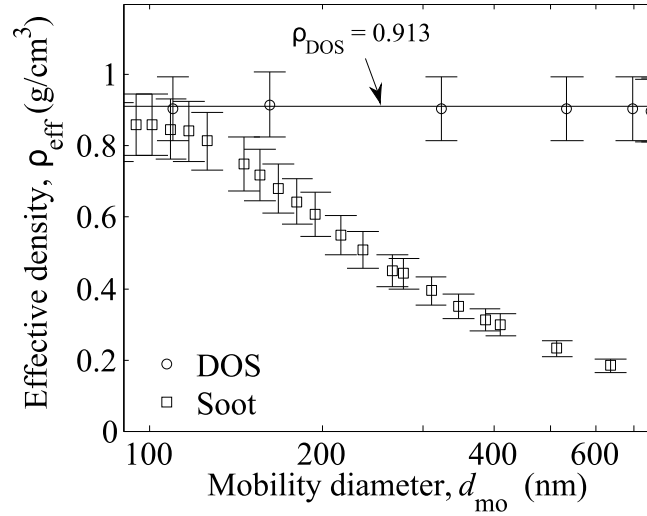


Figure 4. 4 Effective density of soot, DOS and PSL particles.

4.3.3 Dynamic shape factor

The effect of an irregular shape on the drag force of a particle is expressed as the dynamic shape factor. It was first introduced by Fuchs (1964), and can be defined as (Hinds 1999):

$$\chi = \frac{F_D}{F_{D,ve}}, \quad (4.8)$$

where F_D is drag force on the nonspherical particle and $F_{D,ve}$ is the drag force on its volume equivalent sphere¹, when both move at the same relative velocity with respect to the gas. The general equation for drag force on a particle is:

$$F_D = \frac{3\pi\mu v \chi d_{ve}}{C_c(d_{ve})}. \quad (4.9)$$

where v is velocity of particle respect to the gas. In an electric field at a steady velocity, the drag force and the electric force are equal to:

¹This definition can be used to define a dynamic shape factor that includes or excludes internal voids within the particle.

$$F_D = F_e = neE. \quad (4.10)$$

Electrical mobility, Z_p , is defined as the migration velocity of a particle per unit electric field. Therefore, from Equation 4.9 and 4.10 we obtain:

$$Z_p = \frac{neC_c(d_{ve})}{3\pi\mu\chi d_{ve}}. \quad (4.11)$$

Also, electrical mobility equivalent diameter is defined as the diameter of a spherical particle having the same electrical mobility as the particle under consideration (Flagan 2001),

$$Z_p = \frac{neC_c(d_m)}{3\pi\mu d_m}. \quad (4.12)$$

From Equation 4.11 and 4.12 we can demonstrate the relationship between mobility and volume equivalent diameter:

$$\frac{C_c(d_{ve})}{d_{ve}\chi} = \frac{C_c(d_m)}{d_m}. \quad (4.13)$$

The aerodynamic equivalent diameter is defined as the diameter of a spherical particle with a density of 1000 kg/m^3 that has the same terminal settling velocity as the actual particle. For spherical particle with a density of $\rho_0 = 1000 \text{ kg/m}^3$, drag force balance can be written as,

$$\rho_0 \frac{\pi}{6} d_{ae}^3 = \frac{3\pi\mu v_{TS} d_{ae}}{C_c(d_{ae})}. \quad (4.14)$$

The terminal settling velocity can also be written for a non-spherical particle using the definition of the dynamic shape factor and volume equivalent diameter given above:

$$F_D = \rho_p \frac{\pi}{6} d_{ve}^3 = \frac{3\pi\mu v_{TS} \chi d_{ve}}{C_c(d_{ve})} \quad (4.15)$$

where ρ_p is the density of particle including internal voids. By combining Equations 4.14 and 4.15 it can be shown that,

$$v_{TS} = \frac{\rho_p C_c(d_{ve}) d_{ve}^2}{18\mu\chi} = \frac{\rho_0 C_c(d_{ae}) d_{ae}^2}{18\mu}. \quad (4.16)$$

Therefore the relationship between the aerodynamic diameter and volume equivalent diameter is (DeCarlo et al., 2004):

$$d_{ae} = d_{ve} \sqrt{\frac{1 \rho_p C_c(d_{ve})}{\chi \rho_0 C_c(d_{ae})}}. \quad (4.17)$$

The combination of Equation 4.13 and 4.17 gives the relation between mobility diameter, d_{mo} , and aerodynamic diameter, d_{ae} . Therefore, by having d_{mo} and d_{ae} of a particle, the shape factor, χ , and the volume equivalent diameter, d_{ve} , can be calculated.

Park et al. (2004) showed that the material density for diesel soot particles is $1.77 \pm 0.07 \text{ g/cm}^3$, after volatile organics were removed from the particle. Assuming particles do not have internal voids, material density can be used as the particle density, ρ_p . Soot particles aggregate and form larger clusters. These clusters have a fractal-like shape which consists of primary or monomer particles. Figure 4.5 shows that soot particles have shape factors in the range of 1.5 to 2.6 in the range of 95 to 637 nm in mobility diameter. Fractal aggregates occur because of random aggregation of aerosol particles. The shape factor is a function of the monomer and overall aggregate size. Larger aggregates can reach higher aspect ratios hence the larger shape factor. The shape factor for DOS droplets is also shown in the Figure 4.5. The mean value of the shape factor of DOS was 1.03 ± 0.047 , which is within the uncertainty of the expected value of 1.

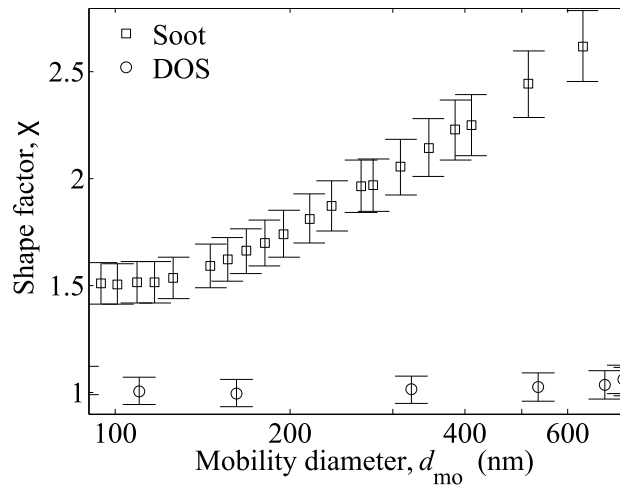


Figure 4. 5 Shape factor of soot and DOS particles.

4.4 Conclusion

The combination of two classifiers has been used to measure other particles properties. In this chapter, a tandem AAC-DMA is used to measure aerodynamic diameter and mobility diameter. This allows one to calculate dynamic shape factor, effective density, mass, and the mass-mobility exponent.

AAC classifies particles aerodynamically with no dependence on the electrical charge state of the particles. In most cases the data interpretation of classifiers that rely on charged particles, requires knowledge of the multiple charged particles and particles charge distribution. The charge correction can lead to ambiguity in the interpretation of the results, especially when both classifiers depend on charged particles; eg. DMA-APM or DMA-CPMA. In tandem AAC-DMA, since the AAC produces a truly monodisperse aerosol, the single and multiple charged particles from DMA are easily distinguishable.

Mass of particles can be measured using the definition of particle relaxation time as the particle's mobility multiplied by particle's mass. Particle relaxation time is measured with an AAC and mobility is measured with a DMA.

From mass and mobility diameter, measured with DMA, effective density can be calculated. Assuming that particles do not have internal voids, the dynamic shape factor can be calculated by combining the relationship between aerodynamic diameter and volume with the relationship between mobility diameter and volume equivalent diameter.

To verify this tandem system, soot and DOS particles were measured. Soot particles were generated from an inverted burner and the mass–mobility exponent of the soot generated from the inverted burner was determined to be 2.17 and for DOS droplets 3.01. The effective density of soot generated from the burner decreases for larger particles because larger particles have higher shape factors. The effective density dropped from 0.86 to 0.18 g/cm³ over the range of 95 to 637 nm in mobility diameter (and the shape factor increased from 1.5 to 2.6 over the same range). The effective density of the DOS particles was equivalent to the material density because they are spherical as also indicated by the measurement of the dynamic shape factor.

Reference

- Ahlvik, P., Ntziachristos, L., Keskinen, J., and Virtanen, A. (1998). Real time measurements of diesel particle size distribution with an electrical low pressure impactor. *Society of Automotive Engineers*. 980410.
- Allen, M. D., Moss, O. R., and Briant, J. K. (1979). Dynamic Shape Factors for LMFBR Mixed-Oxide Fuel Aggregates, *Journal of Aerosol Science* 10(1):43–48.

-
- Coderre, A. R., Thomson, K. A., Snelling, D. R., and Johnson, M. R. (2011). Spectrally Resolved Light Absorption Properties of Cooled Soot from a Methane Flame. *Applied Physics*, B, 104:175–188.
- DeCarlo, P. F., Slowik, J. G., Worsnop, D. R., Davidovits, P., and Jimenez, J. L. (2004). Particle morphology and density characterization by combined mobility and aerodynamic diameter measurements. Part 1: Theory. *Aerosol Science and Technology*, 38:1185–1205.
- Friedlander, S. K. (2000). *Smoke, Dust, and Haze: Fundamentals of Aerosol Dynamics*. Oxford University Press.
- Fuchs, N. A. (1964). *The Mechanics of Aerosols*. Pergamon, New York.
- Ghazi R., Tjong H., Soewono A., Rogak S. N. Olfert, J. S. (2013). Mass, Mobility, Volatility, and Morphology of Soot Particles Generated by a McKenna and Inverted Burner, *Aerosol Science and Technology*, 47:395–405.
- Ghazi, R. and Olfert, J. S., (2013). Coating Mass Dependence of Soot Aggregate Restructuring due to Coatings of Oleic Acid and DioctylSebacate, *Aerosol Science and Technology*, 47:192–200.
- Hand, J. L. and Kreidenweis, S. M. (2002). A new method for retrieving particle refractive index and effective density from aerosol size distribution data. *Aerosol Science and Technology*, 36:1012–1026.
- Hinds, W. C. (1999). *Aerosol Technology—Properties, Behavior, and Measurement of Airborne Particles*. 2nd ed. John Wiley & Sons, New York.
- Kasper, G. (1982a). Dynamics and Measurement of Smokes. Size Characterization of Non-Spherical Particles, *Aerosol Science and Technology*, 1(2):187–199.

-
- Kasper, G. (1982b). Dynamics and Measurement of Smokes. 2. The Aerodynamic Diameter of Chain Aggregates in the Transition Regime, *Aerosol Science and Technology*, 1 (2):201–215.
- Kelly, W. P., and McMurry, P. H. (1992). Measurement of Particle Density by Inertial Classification of Differential Mobility Analyzer–Generated Monodisperse Aerosols, *Aerosol Science and Technology*. 17:199–212.
- Larriba, C., Hogan, C. J. Jr., Attoui, M., Borrajo, R., Garcia, J. F., and de la Mora, J. F. (2011). The Mobility–Volume Relationship below 3.0 nm Examined by Tandem Mobility–Mass Measurement. *Aerosol Science and Technology*, 45(4):453–467.
- Liu, B. Y. H., Pui, D. Y. H., Whitby, K. T., Kittelson, D. B., Kousaka, Y., and McKenzie, R. L. (1978). The Aerosol Mobility Chromatograph: A New Detector for Sulfuric Acid Aerosols, *Atmospheric Environment*. 12:99–104.
- McMurry, P. H., Wang, X., Park, K., and Ehara, K. (2002). The Relationship between Mass and Mobility for Atmospheric Particles: A New Technique for Measuring Particle Density, *Aerosol Science and Technology* 36:227–238.
- Maricq, M. M., Podsiadlik, D. H., and Chase, R. E. (2000). Size distributions of motor vehicle exhaust PM: A comparison between ELPI and SMPS measurements. *Aerosol Science and Technology*, 33:239–260.
- Maricq, M. M. and Xu, N. (2004). The effective density and fractal dimension of soot particles from premixed flames and motor vehicle exhaust. *Journal of Aerosol Science*, 35:1251–1274.
- Olfert, J. S., Symmonds, J. P. R., and Collings, N. (2007). The Effective Density and Fractal Dimension of Particles Emitted from a Light-Duty Diesel

-
- Vehicle with a Diesel Oxidation Catalyst, *Journal of Aerosol Science*, 38:69–82.
- Park, K., Cao, F., Kittelson, D. B., and McMurry, P. H. (2003). Relationship Between Particle Mass and Mobility for Diesel Exhaust Particles, *Environmental Science and Technology*. 37(3):577–583.
- Park, K., Kittelson, D. B., and McMurry, P. H. (2004a). Structural Properties of Diesel Exhaust Particles Measured by Transmission Electron Microscopy (TEM): Relationships to Particle Mass and Mobility, *Aerosol Science and Technology*, 38(9):881–889.
- Park, K., Kittelson, D. B., Zachariah, M. R., and McMurry, P. H. (2004b). Measurement of Inherent Material Density of Nanoparticle Agglomerates, *Journal of Nanoparticle Res.* 6(2–3):267–272.
- Park, K., Dutcher, D., Emery, M., Pagels, J., Sakurai, H., Scheckman, J., Qian, S., Stolzenburg, M., Wang, X., Yang, J. and McMurry, P. H., (2008), Tandem measurements of aerosol properties - A review of mobility techniques with extensions, *Aerosol Science and Technology*, 42 (10), 801-816.
- Rader, D. J., and McMurry, P. H. (1986). Application of the Tandem Differential Mobility Analyzer to Studies of Droplet Growth or Evaporation, *Journal of Aerosol Science*, 17:771–787.
- Rader, D. J., McMurry, P. H., and Smith, S. (1987). Evaporation Rates of Monodisperse Organic Aerosols in the 0.02 to 0.2 μm Diameter Range, *Aerosol Sci. Technol.* 6:247–260.
- Ristimäki, J., Virtanen, A., Marjamäki, M., Rostedt, A., and Keskinen, J. (2002). On-line measurement of size distribution and effective density of submicron aerosol particles, *Journal of Aerosol Science*, 33:1541–1557.

-
- Sorensen, C. (2011). The Mobility of Fractal Aggregates: A Review. *Aerosol Science and Technology*, 45(7):755–769.
- Stipe, C., Higgins, B., Lucasa, D., Koshland, C., and Sawyer, R. (2005). Inverted Co-Flow Diffusion Flame for Producing Soot. *Rev. Sci. Instrument*, 76:023–908.
- Tavakoli, F., and Olfert, J. S. (2013). An Instrument for the Classification of Aerosols by Particle Relaxation, Time: Theoretical Models of the Aerodynamic Aerosol Classifier, *Aerosol Science and Technology*, 47:8, 916-926.
- Virtanen, A., Ristimäki, J., and Keskinen, J. (2004a). Method for measuring effective density and fractal dimension of aerosol agglomerates. *Aerosol Science and Technology*, 38(5):437–446.
- Virtanen, A., Ristimäki, J., Marjamäki, M., Vaaraslahti, K., Keskinen, J., and Lappi, M. (2002). Effective density of diesel exhaust particles as a function of size. *Society of Automotive Engineers*, 01-0056.
- Virtanen, A. K. K., Ristimäki, J. M., Vaaraslahti, K. M., and Keskinen, J. (2004b). Effect of engine load on diesel soot particles, *Environmental Science and Technology*, 38:2551–2556.

Chapter 5

Conclusions and Future Work

The concept of size for non-spherical particles with various shapes must be defined. Therefore, various equivalent diameters are defined to describe the non-spherical particle size. Every equivalent diameter is defined according to a specific physical property which corresponds to a specific measurement technique. When the aerodynamic diameter of a particle is known, particle trajectory can be described independent of particle morphology and density. This makes aerodynamic diameter widely applicable.

Most naturally-produced aerosols are polydisperse and cover more than two orders of magnitude in size. Aerosol classifiers are used to separate a narrow range of particles (monodisperse) from a wider size distribution of particles.

Although there are several methods to measure the aerodynamic diameter of a particle, there has been little success making a practical instrument that produces a monodisperse aerosol classified by aerodynamic diameter. A new instrument called aerodynamic aerosol classifier (AAC) is introduced to classify

particles aerodynamically. The AAC does not rely on particle charging; therefore, it produces a true monodisperse aerosol without classifying multiply-charged particles like the DMA, CPMA, or APM.

Two diffusion models and two non-diffusion models have been used to predict the performance of the AAC. Theoretical transfer function of the AAC has been studied for different conditions.

A prototype of aerodynamic aerosol classifier (AAC) was designed and constructed to show the feasibility of the instrument. PSL (polystyrene latex) particles and DOS (DioctylSebacate) were used to calibrate the instrument. A differential mobility analyzer DMA, and a condensation particle counter (CPC) were used to examine the experimental transfer function and to obtain the penetration efficiency of the AAC.

Another goal of this project was to use a DMA and an AAC in tandem to measure the other properties. Measuring aerodynamic diameter and mobility diameter allows calculating dynamic shape factor, effective density, mass, and mass-mobility relationship. Using tandem DMA-AAC, the aforementioned properties of soot particles emitted from an inverted burner were measured in this study.

5.1 Conclusions and discussion

5.1.1 Theoretical conclusions

In chapter 2, theoretical transfer function of the AAC is investigated. The AAC classifies particles by their particle relaxation time, and as a result the aerodynamic equivalent diameter of the particles can be calculated. Two diffusion models and two non-diffusion models have been used to predict the transfer

function of the AAC. An analytical limiting trajectory model and a particle streamline model were used predict the non-diffusion transfer function. A numerical convective diffusion model and a diffusing particle streamline model were used to model the effects on particle diffusion on the transfer function. The following conclusions were found in the theoretical study:

- 1) The particle streamline models (diffusion and non-diffusion) neglect the divergence of the centrifugal acceleration field in the classifier, but are able to closely approximate the actual classification in the instrument when the gap between the cylinders is small with respect to the radii of the cylinders. In most practical embodiments of the instrument this is expected to be true.
- 2) Although the limiting trajectory model and the convective diffusion model are more accurate representations of the classification in the instrument, it is expected that the particle streamline models (diffusion and non-diffusion) will be more widely used for the following reasons:
 - a) the streamline model has a simpler form and it is simple to see the relationship between the flow rates and the instrument resolution
 - b) The convective diffusion model is numerical and modern computers require several minutes to calculate the transfer function. The diffusive streamline model is analytical and the transfer function is quickly calculated.
 - c) The streamline models for the AAC have very similar form to the streamline models of the differential mobility analyzer, which are widely used and are familiar to many.

- 3) Like the DMA is it expected that the AAC will often be used with balanced flows ($Q_a=Q_s$ and $Q_{sh}=Q_{exh}$) and with an aerosol to sheath flow ratio of 0.1 ($\beta=0.1$)

5.1.2 Experimental conclusions

In chapter 4, the AAC transfer function experimentally examined. One AAC prototype was built, tested, and compared with non-diffusive particle streamline model developed earlier. The AAC prototype was tested over a range of particle sizes. It was found that the transfer function of the AAC agreed with the theoretical model. From the experimental work, the following conclusions were reached:

- 1) The range of an actual instrument will be dependent on its design. The lower size limit will be sensitive to particle diffusion and the maximum rotational speed obtainable and the upper limit will depend on particle impaction in the inlet and outlet of the classifier.
- 2) The calibration is conducted using data from experiments with PSL particles and DOS droplets. To calibrate the AAC the effective length was introduced to adjust for the transfer function location.
- 3) It was also found efficiency of AAC is generally higher for larger particles and the efficiency changes from 10% to 42% for particles from 95 nm to 910 nm size.

5.1.3 Soot particle measurement

In chapter 4 the aerodynamic diameters and the mobility diameter of soot particles were measured simultaneously with a DMA and an AAC in series. The soot particles were generated from an inverted burner. The following properties

for the soot particles are measured in the range of 95 to 637 nm mobility diameter:

- 1) Mass and mass–mobility exponent: Particle mass is calculated from the aerodynamic diameter and the mobility diameter. The mass–mobility exponent of the soot generated from the inverted burner was 2.17.
- 2) Effective density: The effective density dropped from 0.86 to 0.18 g/cm³ over the range of 95 to 637 nm in mobility diameter. The effective density of soot generated from the burner decrease for larger particles because larger particles are less spherical.
- 3) Dynamic shape factor: Larger aggregates can reach higher aspect ratio hence larger shape factor. The dynamic shape factor for soot particles increased from 1.5 to 2.5 in the examined range.

Also, properties of PSL particles and DOS droplets are measured with the same technique. The results confirm the spherical shape of the PSL and DOS particles.

5.2 Future work

The AAC introduced a new method to classify particles size. However, further research could be carried out to improve the performance and functionality of the AAC.

Following is to be considered for the future work:

- 1) *Re-designing the inlet and outlet*: Experimental results shows that with the current AAC design 60% to 90% of particles are lost due to

impaction and diffusion. Impaction is more critical in the corners and inlet and outlet of aerosol and sample flow. Thus, re-designing the inlet and outlet will increase the penetration efficiency.

- 2) *Designing the AAC for two different ranges:* Since different limitations rise to cover and wide range particle size, it is more practical to design two AAC for different particle ranges. Author suggests that one design for larger particles 0.5 to 10 μm and another 10 to 500 nm will improve the functionality of the AAC.
- 3) *Scanning AAC:* Theoretical and experimental study to calculate the transient transfer function of the instrument. This will allow measurement with unsteady rotational speed and provide the ability to scan a wide range of particle sizes quickly (similar to an SMPS).

Appendix A

Particle Relaxation Time as a Function of Aerodynamic Diameter

Solving Stokes's law for the terminal settling velocity V_{TS} gives,

$$V_{TS} = \frac{C_c(d_{ve})\rho_p d_{ve}^2 g}{18\mu} \quad (\text{A.1})$$

where μ is the viscosity of the carrier gas, g is the gravity, C_c is the Cunningham slip correction factor, and d_{ve} is the called volume equivalent diameter of the particle. The aerodynamic equivalent diameter, d_{ae} , is defined as the diameter of a spherical particle with a density of 1000 kg/m^3 that has the same terminal settling velocity as the actual particle.

$$V_{TS} = \frac{C_c(d_{ve})\rho_p d_{ve}^2 g}{18\mu} = \frac{C_c(d_{ae})\rho_0 d_{ae}^2 g}{18\mu} \quad (A.2)$$

The product of the mass, m , and mobility, B , is called relaxation time, τ ,

$$\tau \equiv Bm \quad (A.3)$$

Also, the particle mobility is defined as

$$B \equiv \frac{V}{F_D} \quad (A.4)$$

where V is the particle velocity and the F_D is the drag force. For settling velocity when the drag force equals to gravity force, the terminal velocity, will be

$$V_{TS} = mgB \quad (A.5)$$

Therefore using equation Eq. A.3 and Eq. A.5 gives

$$\tau = \frac{V_{TS}}{g} \quad (A.6)$$

Substituting Eq. A.6 gives

$$\tau = \frac{C_c(d_{ae})\rho_0 d_{ae}^2}{18\mu} \quad (A.7)$$

Aerosols are suspension of liquid or solid particles in a gas. They are formed either by gas-to-particle conversion or by the disintegration of solids or liquids.

Appendix B

Geometric Factor for AAC

The geometric factor G_{AAC} is the non-dimensionalized integral of $v^2 r^2 dt$ in an annular cross section, where t is time (Stolzenburg and McMurry, 2008). G_{DMA} (Stolzenburg (1988); Appendices B and C) can be rearranged for AAC as:

$$G_{AAC} = \left\{ 4(1 + \beta)^2 [I_\gamma(\alpha_s) - I_\gamma(\alpha_a)] + \frac{\alpha_a - \alpha_s}{\kappa^2} \right\} / (1 - \gamma) \quad (\text{B.1})$$

where

$$\begin{aligned} I_\gamma(\alpha) = & A_\gamma^2 (1 - \gamma)^{-1} \\ & \times \{ -\alpha^2 [(1 - \gamma) \ln \alpha - (1 - \alpha) \ln \gamma]^2 / 2 \\ & + [\alpha^2(1 - \gamma)/2 + \alpha^3 \ln \gamma / 3] [(1 - \gamma) \ln \alpha - (1 - \alpha) \ln \gamma] \\ & + (1 + \alpha^2)(1 - \gamma)^2 / 4 + 5(1 - \alpha^3)(1 - \gamma) \ln \gamma / 18 \\ & + (1 - \alpha^4) \ln^2 \gamma / 12 \} \end{aligned} \quad (\text{B.2})$$

and

$$\kappa = r_2 L / (r_2^2 - r_1^2) \quad (\text{B.3})$$

$$\gamma = (r_1 / r_2)^2 \quad (\text{B.4})$$

$$\alpha = (r / r_2)^2 \quad (\text{B.5})$$

α_a and α_s can be calculated by

$$F_\gamma(\alpha_s) = \beta(1 - \delta) / 2(1 + \beta) \quad (\text{B.6})$$

$$1 - F_\gamma(\alpha_a) = \beta(1 + \delta) / 2(1 + \beta)$$

where F_γ is

$$F_\gamma(\alpha) = \frac{[(1 - \alpha)^2 \ln \gamma / 2(1 - \gamma) + \alpha \ln \alpha + (1 - \alpha)]}{[(1 + \gamma) \ln \gamma / 2 + (1 - \gamma)]} \quad (\text{B.7})$$

Reference

Stolzenburg, M. R. and McMurry, P. H. (2008). Equations Governing Single and Tandem DMA Configurations and a New Lognormal Approximation to the Transfer Function, *Aerosol Science and Technology*, 42:6, 421-432.

Appendix C

Aerosol Penetration in Microchannels¹

New applications involving aerosol transport in microscale configurations requires the derivation of the penetration efficiency of microchannels. Although many analytical solutions for the aerosol penetration in channels have been investigated, none of them are applicable for microchannels. Previously, the no-slip condition for the gas velocity and the zero particle concentration at the walls has been applied to the convection diffusion equation. However, recent studies show these boundary conditions may not be appropriate for microscale geometries. The particle penetration through rectangular microchannels and cylindrical microtubes have been obtained using the numerical Crank Nicolson method with slip flow at the walls. Then, existing correlations for the aerosol penetration are modified for the slip flow regime based on an optimization method. These correlations give the penetration as a function of the dimensionless deposition factor and Knudsen number of the gas. At large Knudsen numbers the

¹ The contents of this appendix is published as:
Tavakoli, F., Mitra, S. K, Olfert, J. S. (2011). Aerosol penetration in microchannels, *Journal of Aerosol Science*, 42 (5), pp. 321-328.

penetration decrease to the case relative with continuum flow. The aerosol penetration decreases in the slip flow regime. However, the nonzero boundary condition for the particle concentration at the walls does not have any significant effect on the particle penetration.

C.1 Introduction

The emergence of research on aerosols in microscale configurations requires a new investigation of aerosol transport in microchannels. In the last few years, number of researchers has investigated different applications involving aerosols in microchannels. Akhatov et al. (2008) experimentally studied aerosol flow through a converging micro-capillary in order to focus an aerosol stream. The micro-capillary was of diameter 100 μm and of length 1 cm. Kockmann et al. (2008) investigated aerosol generation and handling in microchannels of a micromixer. A T-shaped micromixer was used for the generation of nanoscale aerosols by the mixing of hot vapor-gas-mixtures with cold gas. In the micromixer, the deposition of particles happens primarily in the bent and disturbed flow. Kwon et al. (2009) demonstrated a micro-machined nano-electrical mobility analyzer (NEMA) for classifying ultrafine aerosol according to their electrical mobility. The micromachined NEMA is based on a rectangular channel with dimensions 4 mm \times 0.5 mm \times 15 mm. However in these systems loss of particles due to diffusion in the microchannels can have a significant effect on results.

The particle transport in microscale configurations can be described by the convection diffusion equation (Friedlander, 2000), which is an Eulerian description of particle motion in flow. In the past many researchers have

investigated the particle loss due to diffusion in tubes and channels where the gas flow is in the continuum regime.

Gormley and Kennedy (1949) proposed two equations for the aerosol penetration through a circular tube for two ranges of the dimensionless deposition factor. Penetration is defined as the fraction of particles that exit after passing through the channel.

Mercer and Mercer (1970) made a theoretical study of particle loss due to diffusion from a fluid flowing radially inward between concentric parallel circular plates. The penetration through the plates was expressed as a function of the dimensionless deposition factor. This function is in the form of an exponential series. The same equation can be applied to parallel flow through a rectangular cross-section by defining an appropriate deposition factor.

Tan and Thomas (1972) investigated convection diffusion phenomena in a channel with parallel walls. The equation was expressed in twenty Eigenconstants, which gives a more accurate value for the penetration. The first four terms of the equation are identical to the Mercer equations which confirm the accuracy of the Mercer's results.

Ingham (1975) also solved the convection diffusion equation to get the penetration for a rectangular and a circular channel. Relationships were obtained when the flow is Poiseuille or plug. Ingham (1976) investigated the penetration of aerosols in a rectangular channel for small values of deposition factor. Simple expressions for the concentration distributions at small distances down the tube are obtained. The results agree well with the results obtained by numerical results of Poiseuille flow for small distances down the channel.

Bowen et al. (1976) utilized confluent hypergeometric functions to solve the convection diffusion equation for a rectangular and a circular channel. Bowen's evaluation of the results shows that this solution is more accurate than all previous solutions, especially for the penetration through cylindrical tubes. For small values of deposition factor, simple Leveque-type asymptotic solutions are obtained. All these problems have been solved in steady, fully developed, laminar flow.

Mathematically, the heat conduction equation and the convection diffusion equation are the same, only the thermal diffusivity replaces the diffusion coefficient. Thus, the heat conduction solutions, available in standard text books like Carslaw and Jaeger (1959) can be used as a solution for convection diffusion problems.

New theoretical studies for nanoparticles with diameter of 20 nm or less show the concentration of particles at the walls does not approach to zero, but has a value proportional to the particle flux to the wall (Gallis et al., 2008a,b). This nonzero boundary condition may become important when the stopping distance of the particle obtained by its thermal velocity is comparable to the geometric length scale. This condition occurs when the operating pressure is low or when the geometric length of the problem is in the microscale.

Although many analytical and semi-analytical solutions for this type of parabolic partial differential equations have been proposed (Gormley and Kennedy, 1949; Carslaw and Jaeger, 1959; Mercer and Mercer, 1970; Tan and Thomas, 1972; Ingham, 1975; Bowen et al., 1976), none of them have been modified for microscale geometries. Thus, new boundary conditions should be

applied for the velocity profile and the particle concentration at the walls. Previously, no-slip conditions for the velocity and zero particle concentration at the walls have been applied to the convection diffusion equation. However, these boundary conditions are not appropriate for micro-scale geometries and nanoparticle aerosols. These very important understanding of the micro-scale phenomena in form of modified boundary conditions have been incorporate in the present work. Finally, we will develop an expression for the penetration efficiency of aerosols in rectangular microchannels and cylindrical microtubes, the two representative geometries commonly used in aerosol applications.

C.2 Theory

A schematic view of a rectangular microchannel (two infinite parallel plates) and a microtube (cylindrical microtube) is shown in Fig. C.1. The rectangular microchannel is of width W with a separation h , where $h \ll W$ and the microtube is of radius r_0 and the microchannels are of length L .

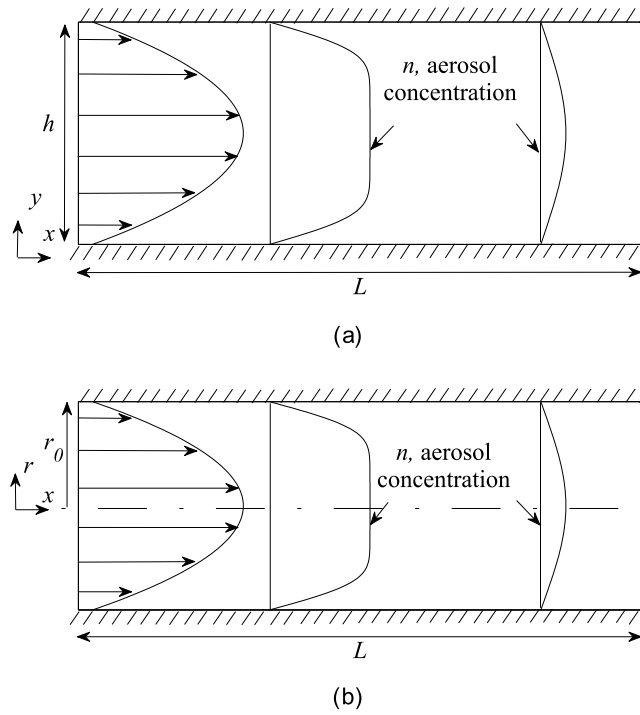


Figure C. 1 Schematic of microchannels, (a) a rectangular microchannel and (b) a microtube.

The gas flow in the microchannels is in the slip flow regime, where $0.01 \leq \text{Kn} \leq 0.1$, therefore, the velocity of the gas at the wall is non-zero. Kn is the Knudsen number, which is defined as the gas mean free path, λ , to the characteristic length - h for microchannels and $2r_0$ for microtubes². The flow in the channels is considered incompressible and fully developed³. Accounting for the second order slip velocity on the walls, the velocity profile for the flow inside the microchannel can be written as (Karniadakis et al., 2000):

² This is the Kn defined for the microchannel and not the Kn_p defined for the particle as defined in Eq. (C.4).

³ In most applications the entrance length can be neglected relative to the channel length. Expressions for the entrance length in circular and noncircular microchannels are given by Duan and Muzychka (2010).

$$v_x(y) = \frac{h^2}{2\mu_g} \frac{dp}{dx} \left[\frac{y^2}{h^2} - \frac{y}{h} + \frac{2 - \sigma_v}{\sigma_v} (\text{Kn}^2 - \text{Kn}) \right]. \quad (\text{C.1})$$

Similarly, for the microtube the velocity can be expressed as (Karniadakis et al., 2000):

$$v_x(r) = \frac{r_0^2}{4\mu_g} \frac{dp}{dx} \left[\left(\frac{r}{r_0} \right)^2 - 1 - \frac{2 - \sigma_v}{\sigma_v} (4\text{Kn}^2 - 4\text{Kn}) \right]. \quad (\text{C.2})$$

Here, μ_g is the gas viscosity; p is the pressure and σ_v is the tangential momentum accommodation coefficient. Here, $\sigma_v = 1$ through diffuse reflection approximation (Karniadakis et al., 2000), which depicts the tangential momentum exchange of the gas with the walls.

The particle concentration distribution at the beginning of the channel is considered uniform. It is assumed that the concentration of particles in the flow is low so that coagulation and the effect of particles on the flow are neglected. These particles transport in the flowing fluid by convection and diffusion. The diffusion coefficient, D , has been described in terms of the particle Brownian motion by Einstein (1905):

$$D = kTB = \frac{kT}{3\pi\mu_g d_p} \quad (\text{C.3})$$

where k is Boltzmann's constant, T is the temperature, d_p the particle diameter, and B is particle mobility. For small particle sizes the particle mobility has been corrected by the slip correction, C_C , and diffusion can be written as $D = kTC_C/3\pi\mu_g d_p$. The slip correction is given by Allen and Raabe (1985):

$$C_c = 1 + \text{Kn}_p \left[1.257 + 0.4 \exp\left(-\frac{1.1}{\text{Kn}_p}\right) \right]. \quad (\text{C.4})$$

where Kn_p is the particle Knudsen number defined as $2\lambda/d_p$. The convection diffusion equation for incompressible flow with constant diffusion coefficient is given by the following equation (Friedlander, 2000):

$$\frac{\partial n}{\partial t} + \mathbf{v} \cdot \nabla n = D \nabla^2 n - \nabla \cdot \mathbf{u}_d n, \quad (\text{C.5})$$

where

$$\mathbf{u}_d = \mathbf{F}_{\text{ext}} B. \quad (\text{C.6})$$

Here, n is the particle concentration, \mathbf{v} is the gas velocity, \mathbf{F}_{ext} is the external force acting on the particles and \mathbf{u}_d is the migration or drift velocity in the field, which equals to $\mathbf{u}_p - \mathbf{v}$, the difference between particle and gas velocities.

Aerosol particles deposit on a surface due to the presence of attractive London-van der Waals force between particles and the surface (Friedlander, 2000). Hence, conventionally in aerosol science the concentration of particles at a wall is considered to be zero which is a very good approximation for common aerosol particles. But new studies with nanoparticle aerosol of size 20 nm and less show that this approximation may not be always true (Gallis et al., 2008b). Theoretical investigations show that the concentration at a wall is a nonzero value but proportional to the flux of particles to the wall, which can be written as (Gallis et al., 2008b,a)

$$\hat{\mathbf{n}} \cdot \left(n \mathbf{u}_d - D \frac{\partial n}{\partial \mathbf{x}} \right) = \frac{ncf}{\pi^{1/2}}, \quad (\text{C.7})$$

where $c = (2kT/m)^{1/2}$ and f is the particle flux coefficient which can be determined by:

$$f = s \left\{ 2 - s \left[1 + \operatorname{erf}(u^*) - \frac{1 - \exp(-u^{*2})}{\pi^{1/2} u^*} \right] \right\}^{-1}. \quad (\text{C.8})$$

Here, s is the sticking fraction which is the probability that a particle will stick to the wall. Furthermore, $u^* = u_d/c$ and $u_d = \mathbf{u}_d \cdot \hat{\mathbf{n}}$, with $\hat{\mathbf{n}}$ as the normal vector toward the walls. In the absence of external forces and the consequent drift velocity, the particle flux equation can be simplified as:

$$f = \frac{s}{2 - s}. \quad (\text{C.9})$$

The nonzero boundary condition equations are obtained using theoretical analysis based on the generalized Fokker-Planck equation and Brownian motion simulated by the Langevin equation (Gallis et al., 2008a). The nonzero boundary condition for particle concentration is applied when the characteristic length is comparable to the thermal stopping distance l , which happens when the pressure is low or the scale of problem is in the microscale. The thermal stopping distance for a particle is given by:

$$l = \frac{\pi^{1/2}}{2} c\tau, \quad (\text{C.10})$$

where $\tau = mB$ is the particle relaxation time, and m is the particle mass.

C.3 Methodology

The convection diffusion equation can be rewritten for a two-dimensional fully developed flow in a channel without any external force. Here diffusion in the

x-direction is neglected compared to the diffusion term in the y- or r-direction and the convection term in the x-direction. The non-dimensional equation then can be written for the two representative geometries as:

$$\frac{\partial n^*}{\partial x^*} = \frac{DL}{v_x(y^*)h^2} \frac{\partial^2 n^*}{\partial y^{*2}}, \quad (\text{C.11})$$

$$\frac{\partial n^*}{\partial x^*} = \frac{DL}{v_x(r^*)r_0^2} \left(\frac{\partial^2 n^*}{\partial r^{*2}} + \frac{1}{r^*} \frac{\partial n^*}{\partial r^*} \right), \quad (\text{C.12})$$

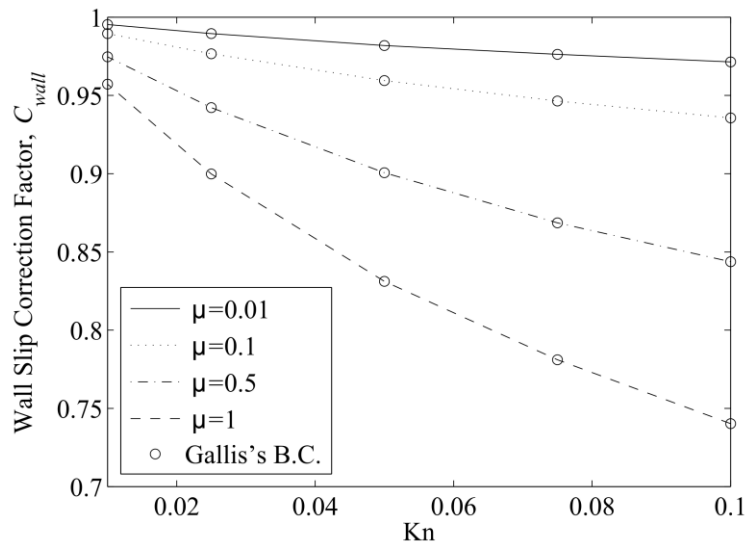
where $x^* = x/L$, $y^* = y/h$ and $r^* = r/r_0$ are non-dimensional lengths. Also, $n^* = n/n_0$ is the nondimensionalized particle concentration where n_0 is the initial particle concentration. In this case the solution to the convection diffusion equation only depends on $DL/v_x h^2$ or $DL/v_x r_0^2$. In order to solve Eqs. C.11 and C.12, the implicit Crank Nicolson method for finite discretization has been used (Smith, 1978). The Crank Nicolson method is a finite difference method usually used for solving the heat and other diffusion equations. This method is unconditionally stable for diffusion equations, therefore, dimensions of the grid can be chosen freely. This method converges faster than other explicit methods and gives second-order accuracy in all dimensions.

C.4 Results and discussion

C.4.1 Effect of slip flow at the walls on the penetration

As mentioned earlier, the penetration through a channel has been derived by others as a function of deposition factor μ , a dimensionless argument, which is related to the diffusion coefficient, channel length, height and the flow velocity. For a channel, the deposition factor μ can be defined as $8DL/\bar{v}_x h^2$ and for a tube as $DL/\bar{v}_x r_0^2$ (Baron and Willeke, 2001).

For microchannels, the conventional gas flow equations are not valid because the gas velocity profile is different, due to finite slip at the wall. In this case, one can define the wall slip correction factor as $C_{\text{wall}} = P_{\text{slip}}/P_{\text{noslip}}$, the ratio of the particle penetration through a channel with flow in the slip regime to the penetration through the channel in the continuum regime for a fixed μ . Figure C.2 shows the relation of slip correction factor with Knudsen number for rectangular microchannels and microtubes. It is observed that C_{wall} is smaller than one and its value decreases with increase in Kn and μ . In the presence of slip velocity at the walls, convection in the axial direction near the wall increases; however, the convection in the center of the channel decreases for a fixed average velocity. Since the particle concentration in the center of the channel is high, the decrease in the convection in the center of the channel has a more significant effect. Thus, the penetration of the aerosol through the channel with slip flow is smaller than the aerosol penetration without considering slip velocity at the walls. As the Kn increases, the deviations from penetration for continuum model increase; therefore, C_{wall} decreases.



(a)

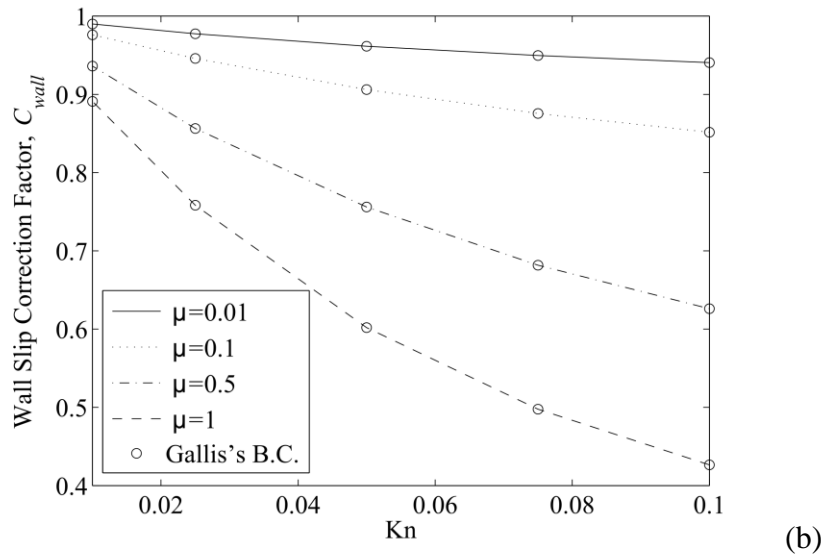


Figure C. 2 Variation of wall slip correction for (a) rectangular microchannels and (b) microtubes for different values of μ . Marked 'o': results by applying the nonzero boundary condition for particle concentration at the walls (Gallis et al., 2008b).

Aerosol penetration through microchannels is obtained by numerical solution of the convection diffusion equation for different Kn and the continuum regime. Figure C.3 shows the penetration through a rectangular channel (3a) and a tube (3b) for the continuum regime and the slip flow regime with $Kn = 0.1$. Also, it is observed that the numerical results agree with Bowen et al. (1976) analytical solution for the continuum regime.

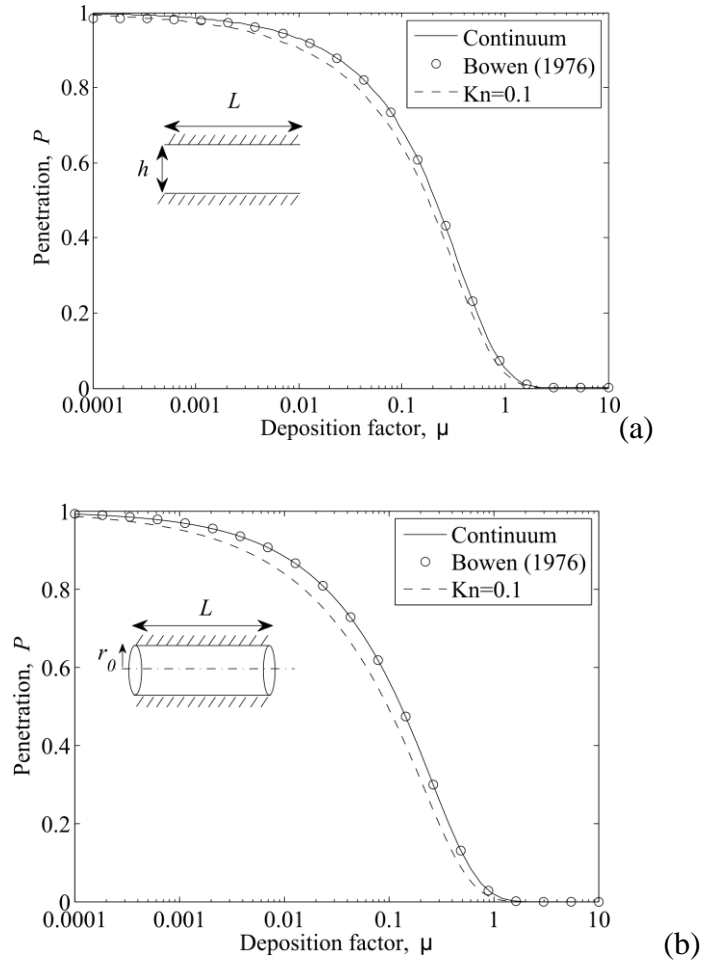


Figure C. 3 Variation of penetration with deposition factor for (a) rectangular channels and (b) cylindrical tubes. Solid line: numerical results for the continuum regime, dashed line: Knudsen number equals 0.1, marked ‘o’: results by Bowen et al. (1976).

C.4.2 Penetration equation

A simple correlation is sought for the penetration as a function of μ and Kn. The correlation for penetration in microchannels for different Kn is obtained as:

$$P = 1 - 1.526\mu_1^{2/3} + 0.15\mu_2 + 0.0342\mu_3^{4/3} \quad \text{for } \mu \leq 0.05 \quad (\text{C.13})$$

$$\begin{aligned}
P &= 0.9104 \exp(-2.8278\mu_4) + 0.0531 \exp(-32.147\mu_5) \\
&\quad + 0.01528 \exp(-93.475\mu_6) \\
&\quad + 0.00681 \exp(-186.805\mu_7) \text{ for } \mu > 0.05
\end{aligned}$$

Similarly, for the microtube, one can obtain a correlation for the penetration as a function of Kn as:

$$\begin{aligned}
P &= 1 - 2.5638\mu_1^{2/3} + 1.2\mu_2 + 0.1767\mu_3^{4/3} \text{ for } \mu \leq 0.02 \\
P &= 0.81905 \exp(-3.6568\mu_4) + 0.09753 \exp(-22.305\mu_5) \\
&\quad + 0.0325 \exp(-56.961\mu_6) \\
&\quad + 0.01544 \exp(-107.62\mu_7) \text{ for } \mu > 0.02
\end{aligned} \tag{C.14}$$

$$\mu_i = \mu(1 + a_i \text{Kn}). \tag{C.15}$$

The values of constant a_i for microchannels and microtubes are given in Table C.1. In the continuum regime μ_i are just equal to μ which reduces to the relations that are given by Gormley and Kennedy (1949); Mercer and Mercer (1970); Tan and Thomas (1972) and Ingham (1976). Equations C.13 and C.14 were obtained using `fminsearch` Matlab function, on the numerical results. `Fminsearch` in Matlab utilizes a derivative-free optimization method (Lagarias et al., 1998). One thousand numerical results have been used for this function optimization. The numerical results are selected from five different Kn and two hundred values μ of in logarithmic scale. In order to obtain the optimized function, different shapes of functions were tested such as different forms and different orders of polynomials. It was found that the simple linear correction provided excellent agreement with the numerical results, without the added

complexity of higher order terms. In fact the maximum deviation of Eqs. C.13 and C.14 from the numerical model is less than 0.3%. These equations are valid for slip flow regime, i.e., $0.01 \leq \text{Kn} \leq 0.1$ with the specified velocity profiles, as depicted by Eqs. C.1 and C.2.

Table C.1: Constant for rectangular microchannels and cylindrical microtubes.

a_i	a_1	a_2	a_3	a_4	a_5	a_6	a_7
Microtube	14.066	178.89	-19.409	1.6911	67.869	17.742	7.9406
Microchannel	23.219	74.639	-18.177	3.4857	29.402	2.0005	136.48

C.4.3 Nonzero particle concentration at the walls

Gallis et al. (2008b) show that for microscale geometries particle concentration at the walls approaches to a nonzero value. Therefore, the effect of this boundary condition on the penetration of microchannels was also investigated. Thus, a nonzero boundary condition for the particle concentration at the walls has been applied. Figure C.4 illustrates the normalized particle concentration at the walls of a channel considering the continuum regime and flow with $\text{Kn} = 0.1$; where s is the sticking fraction. It can be seen that the particle concentration at the walls decreases as s increases. Since particle concentration at the walls is proportional to the particle flux to the walls and particle concentration gradient at the walls, the particle concentration at the walls decreases by increasing μ .

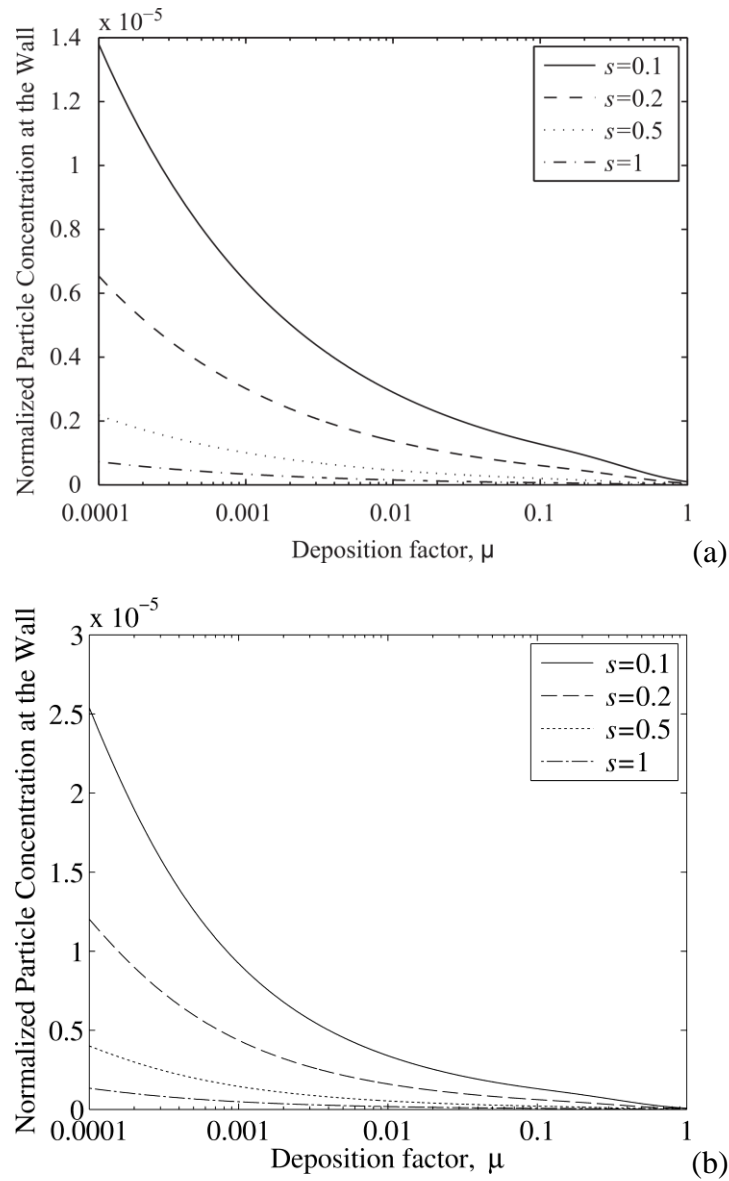


Figure C. 4 Variation of article concentration at the wall for (a) continuum regime and (b) $Kn=0.1$ for a rectangular microchannel.

It is observed that even the case for which the sticking factor s is equal to one, the particle concentration is not zero. However, it is also found that the particle concentration at the walls is in order of 10^{-5} of the particle concentration in the channel inlet, and the nonzero particle concentration at the walls as a boundary condition has almost no effect on particle penetration through the microchannels.

Figure C.2 shows that there is no difference in results obtained by applying Gallis's boundary conditions and the standard zero concentration boundary condition. In fact, the difference in the penetration after considering the nonzero boundary condition is in order of 10^{-7} which is below the numerical accuracy of the present method.

C.5 Conclusion

The diffusion losses of aerosols in microchannels have been studied. The aerosol penetration as the fraction of particles that exit after passing through the channel have been investigated. Analytical solutions for the aerosol penetration in the continuum regime had been investigated previously. However, in this study the gas flow is in the slip flow regime. By considering the slip flow in a channel, convection in the center of the channel decreases; therefore, the penetration decreases for the slip regime. A correlation is developed for the penetration as a function of the dimensionless deposition factor and Knudsen number for rectangular microchannels and cylindrical microtubes.

Also, a nonzero boundary condition for the particle concentration at the walls has been applied in the microchannels. It has been shown that even when the sticking fraction is equal to unity the concentration at the walls does not become zero. However, the magnitude of the particle concentration at the walls is so small that does not have any significant effect on the particle penetration.

Reference

- Akhatov, I., Hoey, J., Swenson, O., and Schulz, D. (2008). Aerosol flow through a long micro-capillary: collimated aerosol beam. *Microfluidics and Nanofluidics*, 5 , 215–224. 10.1007/s10404-007-0239-3.
- Allen, M. D., and Raabe, O. G. (1985). Slip correction measurements of spherical solid aerosol particles in an improved millikan apparatus. *Aerosol Science and Technology*, 4: 3 , 269 – 286.
- Baron, P., and Willeke, K. (2001). *Aerosol Measurement* (2nd ed). John Wiley and Sons: New York.
- Bowen, B. D., Levine, S., and Epstein, N. (1976). Fine particle deposition in laminar flow through parallel-plate and cylindrical channels. *Journal of Colloid and Interface Science*, 54 , 375 – 390.
- Carslaw, H., and Jaeger, J. (1959). *Conduction of Heat in Solids*. Oxford Univ. Press: New York.
- Einstein, A. (1905). Uber die von der molekularkinetischen theorie der warme geforderte bewegung von in ruhenden flussigkeiten suspendierten teilchen. *Annalen der Physik* , 322 , 549560.
- Friedlander, S. (2000). *Smoke, dust and Haze*. Oxford Univ Press.
- Gallis, M. A., Torczynski, J. R., and Rader, D. J. (2008a). Nanoparticle knud-sen layers in gas-filled microscale geometries. *Phys. Rev. E* , 77 , 036302 – 036309.
- Gallis, M. A., Torczynski, J. R., and Rader, D. J. (2008b). Nonzero-concentration boundary condition for advection-diffusion aerosol-transport modeling. *Aerosol Science and Technology*, 42: 10 , 829 – 831.

-
- Gormley, P., and Kennedy, M. (1949). Diffusion from a stream flowing through a cylindrical tube. *Proc. Roy. Irish Academy*, A52 , 163 – 169.
- Ingham, D. (1975). Diffusion of disintegration products of radioactive gases in circular and flat channels. *Journal of Aerosol Science*, 6 , 395 – 402.
- Ingham, D. (1976). Simultaneous diffusion and sedimentation of aerosol particles in rectangular tubes. *Journal of Aerosol Science*, 7 , 373 – 380.
- Karniadakis, G., Beskok, A., and Aluru, N. (2000). *Microflows and Nanoflows Fundamentals and Simulation*. Springer: New York.
- Kockmann, N., Dreher, S., Engler, M., and Woias, P. (2008). Aerosol generation and handling in microchannels. *Chemical Engineering Journal* , 135 , S121 – S125. *Microreaction Technology IMRET 9: Proceedings of the Ninth International Conference on Microreaction Technology - IMRET9 Special Issue*.
- Kwon, S.-M., Kim, Y.-H., Jung, I.-H., Park, D., Hwang, J., and Kim, Y.-J. (2009). Size classification of airborne particle for air-based lab-on-a-chip using micromachined electrical mobility analyzer. *Current Applied Physics*, 9 , e308 – e310. *NanoBio-Seoul 2008*.
- Lagarias, J. C., Reeds, J. A., Wright, M. H., and Wright, P. E. (1998). Convergence properties of the nelder–mead simplex method in low dimensions. *SIAM J. on Optimization*, 9 , 112–147.
- Mercer, T., and Mercer, R. L. (1970). Diffusional deposition from a fluid flowing radially between concentric, parallel, circular plates. *Journal of Aerosol Science*, 1 , 279 – 285.
- Smith, G. D. (1978). *Numerical Solution of Partial Differential Equations: Finite Difference Methods*. Oxford University Press.

Tan, C., and Thomas, J. (1972). Aerosol penetration through a parallel-plate diffusion battery. *Journal of Aerosol Science*, 3 , 39 – 43.

Appendix D

Implementing the Crank-Nicolson Method for the Numerical Diffusion Model of AAC

This appendix shows the Crank-Nicolson method to solve the numerical diffusion model. In Chapter 2 a non-dimensional partial differential equation was derived from the convective-diffusion equations of particles in the AAC:

$$\frac{\partial \tilde{n}}{\partial \tilde{z}} = \frac{1}{2} \eta^2 \frac{\partial^2 \tilde{n}}{\partial \tilde{r}^2} - \zeta \frac{\partial \tilde{n}}{\partial \tilde{r}}, \quad (\text{D.1})$$

The MATLAB code used to solve this equation is shown as follows:

```
clear;
clc;
%%%%%%%%%%%%%% Input physical parameters %%%%%%%%%%%%%%%
Q_sh=3 *1e-3/60; % Sheath flow
Q_a=0.3 *1e-3/60; % Aerosol flow
Q_s=Q_a; % Sample flow
```

```

dp_max_Diff=100e-9;
for t=1:tmax
    n_old = n_0;
    dp(t)=dp_min_Diff+(dp_max_Diff-dp_min_Diff)/tmax*t;
    B=Cc(dp(t),1)/(3*pi*mu*dp(t));
    D=k*T*B;
    tau(t)=B*1000*pi/6*dp(t)^3;
    for j=2:jmax-1      % finding constant coef. in Crank-Nicolson Method
        r(j)= r_1+(y(j)*H);
        beta= L/H^2*D /Uave;
        a(j)=dx/dy/2 *L/H * tau(t)* omega^2*r(j) /(Uave*u(j));
        b(j)=dx/dy^2 *beta /u(j);
    end

    for j=2:jmax-1      % Create the Matrix
        midd(j-1)=1+b(j);
    end
    for j=3:jmax-1
        down(j-2)=-a(j)/2-b(j)/2;
    end
    for j=2:jmax-2
        up(j-1)=-b(j)/2+a(j)/2;
    end

    for i=2:imax      % Marching in x-direction for solving "n"
        for j=1:jmax-2
            if (j==1);rhs(j)=(1-b(j+1))*n_old(j)+(-a(j+1)/2+b(j+1)/2)...
                *n_old(j+1);
            else
                if (j==jmax-2);rhs(j)=(a(j+1)/2+b(j+1)/2)*n_old(j-1)...
                    +(1-b(j+1))*n_old(j);
                else
                    rhs(j)=(a(j+1)/2+b(j+1)/2)*n_old(j-1)+(1-b(j+1))*...
                        n_old(j)+(-a(j+1)/2+b(j+1)/2)*n_old(j+1);
                end
            end
            end
        n_new = tridiag1( down, midd, up, rhs );
        n_old=n_new;
    end

    for j=1:jmax-2      % Outlet flux
        if (1-y(j+1)<(r_2-r_s)/H)
            flux_out(t)=n_old(j-1)*u(j)+flux_out(t);
        end
    end
end
end

```

```

function cun = Cc(d,P)

% This function gives the cunningham slip correction
% factor of particles with diameter d (m) at pressure P (atm)

alpha = 1.142*2;
beta = .558*2;
gamma = .999/2;

la = 66e-9; % mfp of air at atm pressure
lap = la/P; % mfp of air at sub-atm pressure

cun = 1+((lap)./d).*(alpha + beta*exp(-gamma*d/lap));

```

```

function [d_a]=relaxtime2dp_a(tau,P,T)

%This function converts relaxation time to aerodynamic particle size.
% tau = the particle relaxation time
% P = the pressure in atm
% T = the temperature in K

mu=1.81e-5*(T/293)^(0.74); %example after eq.2.29 in Hinds
for j=1:length(tau)
    f=@(d_a)tau(j)-Cc(d_a,P)*1000*d_a^2/18/mu;
%    f=@(d_a)tau(j)-(1+2*66.0e-9/d_a*(1.257+0.4*exp(-
1.1*d_a/(2*66.0e-9))))*1000*d_a^2/18/mu;

    %guess a solution from a fit i did
    guess = 0.0598*tau(j)^0.8345;
    d_a(j) = fzero(f,guess);
end

```

```

function x = tridiag1( a, b, c, y )
%    x = tridiag( a, b, c, y )
%
% Solve the N x N tridiagonal system for x:
%
% [ b(1)  c(1)                ] [ x(1) ] [ y(1) ]
% [ a(1)  b(2)  c(2)          ] [ x(2) ] [ y(2) ]
% [          a(2)  b(3)  c(3) ] [      ] [      ]
% [          ...  ...  ...    ] [ ... ] = [ ... ]
% [          ...  ...  ...    ] [      ] [      ]

```

```

% [          a(N-2) b(N-1) c(N-1) ] [ x(N-1) ] [ y(N-1) ]
% [          a(N-1) b(N)   ] [ x(N)   ] [ y(N)   ]
%
% y must be a vector (row or column); N is determined from its length.
% a, b, c must be vectors of lengths at least N-1, N, and N-1
% respectively,

%%%%%%%%%%%%%%%%%%%%%%%%%%%%%%%%%%%%%%%%%%%%%%%%%%%%%%%%%%%%%%%%%%%%%%%%
% Check that the input arrays have acceptable sizes

if min(size(y))~=1 | min(size(a))~=1 | min(size(b))~=1 | min(size(c))~=1
    error('a, b, c, y must be vectors');
end
N = length(y);
if length(a)<N-1 | length(b)<N | length(c)<N-1
    error('a, b, c must be vectors of length at least N-1, N, N-1');
end

%%%%%%%%%%%%%%%%%%%%%%%%%%%%%%%%%%%%%%%%%%%%%%%%%%%%%%%%%%%%%%%%%%%%%%%%
% Solve the problem by back substitution

gam = zeros(1,N); % hold the LU decomposition
x = zeros(size(y));

% phase 1: LU decomposition
beta = b(1);
if beta==0
    error('beta = 0 at j=1: matrix is singular');
end

x(1) = y(1) / beta;
for j=2:N
    gam(j) = c(j-1) / beta;
    beta = b(j) - a(j-1)*gam(j);
    if beta==0
        error([ 'beta = 0 at j=' num2str(j) ': matrix is singular' ]);
    end
    x(j) = ( y(j) - a(j-1)*x(j-1) )/beta;
end

% phase 2: back-substitution
for j=N-1:-1:1
    x(j) = x(j) - gam(j+1)*x(j+1);
end

```

```
function [r3, r4]=rrp(r1, r2, Qsh , Qa, Qs)
Umax=3/2*(Qsh+Qa) / (pi*((r2)^2-(r1)^2));
f3=@(r3)Qa+8*pi*Umax/(r2-r1)^2*(r1^4/12-r1^3*r2/6+r1*r2*r3^2/2-r1*r3^3/3-
r2*r3^3/3+r3^4/4);
f4=@(r4)Qs+8*pi*Umax/(r2-r1)^2*(r1*r2^3/6-r1*r2*r4^2/2+r1*r4^3/3-
r2^4/12+r2*r4^3/3-r4^4/4);
r3=fzero(f3,[r1,r2]);
r4=fzero(f4,r2);
```

Appendix E

Uncertainty Analysis

In chapter 2 it is shown that the transfer function relaxation time can be calculated by:

$$\tau_{\text{theory}}^* = \frac{2Q_{\text{sh}}}{4\pi\omega^2\bar{r}^2L} \quad (\text{E.1})$$

Applying the propagation of uncertainty methods, gives:

$$\left(\frac{\varepsilon_{\tau^*}}{\tau^*}\right)^2 = \left(\frac{\varepsilon_{Q_{\text{sh}}}}{Q_{\text{sh}} + Q_{\text{exh}}}\right)^2 + 4\left(\frac{\varepsilon_{\omega}}{\omega}\right)^2 + 4\left(\frac{\varepsilon_{\bar{r}}}{\bar{r}}\right)^2 + \left(\frac{\varepsilon_L}{L}\right)^2 \quad (\text{E.2})$$

where $\varepsilon_{Q_{\text{sh}}} = \varepsilon_{Q_{\text{exh}}} = 0.1 \text{ L/hr}$, $\varepsilon_{\omega} = 5 \text{ rpm}$, $\varepsilon_L = 2 \text{ mm}$ and $\varepsilon_{\bar{r}} = 5 \mu\text{m}$. Also, it is shown that the aerodynamic diameter can be calculated from the particle relaxation time:

$$\tau = \frac{C_c(d_{ae})\rho_0 d_{ae}^2}{18\mu}, \quad (E.3)$$

therefore, the uncertainty for the aerodynamic diameter will be

$$\left(\frac{\varepsilon_{d_{ae}}}{d_{ae}}\right)^2 = \sqrt{0.5} \left(\frac{\varepsilon_\tau}{\tau}\right)^2 + \sqrt{0.5} \left(\frac{\varepsilon_\mu}{\mu}\right)^2 + \sqrt{0.5} \left(\frac{\varepsilon_{C_c}}{C_c}\right)^2, \quad (E.4)$$

where ε_μ is calculated from temperature uncertainty of 4°C, therefore, $\varepsilon_\mu/\mu = 1.2\%$. It is assumed that the uncertainty of slip corrections, ε_{C_c}/C_c , is the same for all particle size and equals to 2.1% (Allen and Raabe; 1985).

From the definition of the particle relaxation time,

$$\tau = Bm. \quad (E.5)$$

Similarly the uncertainty for particle mass can be written as:

$$\left(\frac{\varepsilon_m}{m}\right)^2 = \left(\frac{\varepsilon_\tau}{\tau}\right)^2 + \left(\frac{\varepsilon_B}{B}\right)^2, \quad (E.6)$$

where,

$$B = \frac{C_c}{3\pi\mu d_{mo}} \quad (E.7)$$

and,

$$\left(\frac{\varepsilon_B}{B}\right)^2 = \left(\frac{\varepsilon_{C_c}}{C_c}\right)^2 + \left(\frac{\varepsilon_\mu}{\mu}\right)^2 + \left(\frac{\varepsilon_{d_{mo}}}{d_{mo}}\right)^2, \quad (E.8)$$

where $\varepsilon_{d_{mo}}/d_{mo} = 3\%$ (Kinney et al., 1991). Effective density is calculated via following Equation

$$\rho_{\text{eff}} = \frac{m}{\frac{\pi}{6}d_{mo}^3}. \quad (E.9)$$

As a result, the uncertainty of effective density express as

$$\left(\frac{\varepsilon_{\rho_{\text{eff}}}}{\rho_{\text{eff}}}\right)^2 = 9\left(\frac{\varepsilon_{d_{\text{mo}}}}{d_{\text{mo}}}\right)^2 + \left(\frac{\varepsilon_m}{m}\right)^2. \quad (\text{E.10})$$

Since the dynamic shape factor is

$$\chi = \left(\frac{d_{\text{mo}}}{d_{\text{ae}} C_c(d_{\text{mo}})}\right)^{2/3} \frac{\rho_p^{1/3} C_c(d_{\text{ve}})}{\rho_0^{1/3} C_c^{1/3}(d_{\text{ae}})}, \quad (\text{E.11})$$

The uncertainty of dynamic shape factor can be calculated as

$$\left(\frac{\varepsilon_\chi}{\chi}\right)^2 = 4/9\left(\frac{\varepsilon_{d_{\text{mo}}}}{d_{\text{mo}}}\right)^2 + 4/9\left(\frac{\varepsilon_{d_{\text{ae}}}}{d_{\text{ae}}}\right)^2 + 4\left(\frac{\varepsilon_{C_c}}{C_c}\right)^2 + 1/9\left(\frac{\varepsilon_{\rho_p}}{\rho_p}\right)^2 \quad (\text{E.12})$$

Reference:

Allen, M. D., and Raabe, O. G. (1985). Slip correction measurements of spherical solid aerosol particles in an improved millikan apparatus. *Aerosol Science and Technology*, 4: 3, 269 – 286.

Kinney, P. D., Pui, D. Y. H., Mulholland, G. W. and Bryner, N. P. (1991). Use of the Electrical Classification Method to Size 0.1 μm SRM Particles—A Feasibility Study, *J. Res. Natl. Inst. Stand. Technol.*, 96: 147–176.